TWO-TEMPERATURE NATURE OF INTRACLUSTER MEDIUM: SHOCK HEATING AND NONEQUIPARTITION OF ELECTRONS AND IONS

Motokazu Takizawa

Department of Astronomy, Faculty of Science, Kyoto University

Abstract

In part I of this thesis, we summarize the basic concepts concerning clusters of galaxies. We describe the basic physics of gravitational many body systems, which correspond to the dynamical models of galaxies and dark matter in clusters of galaxies. Basic physical properties of intracluster medium are summarized. We briefly review mass estimation, the self-similar model, Sunyaev-Zel'dovich effect, and the relation between cosmological parameters and clusters.

In part II, dynamical evolutions of spherical X-ray clusters of galaxies are studied by using N-body + TVD mesh code. We consider a growth of density perturbation of $10^{15} M_\odot$ composed of dark matter and gas in cold dark matter dominated universe with $\Omega_0 = 1$ or 0.2. When the perturbation collapsed at $z \sim 1$ a shock front appears at $r \sim 0.1$ Mpc, moving outward as ambient gas accretes towards cluster center. The shock front separates the inner X-ray emitting, hot region from the outer cool region. In the former gas is almost in hydrostatic equilibrium but with small radial infall ($\sim 100 \mathrm{km\ s^{-1}}$) being left, while in the latter gas falls almost freely and emits no X-rays. Gas inside the shock is strongly compressed and heated by shock so that X-ray luminosity rapidly rises in the early stage (until temperature reaches about virial). In the late stage, on the other hand, the X-ray luminosity rises only gradually due partly to the expansion of the inner high temperature region and partly to the increase of X-ray emissivity of gas as the results of continuous adiabatic compression inside the shock. We also find that the density distribution is generally less concentrated in a lower density universe and, hence, X-ray luminosity rises more slowly than in a higher density universe.

The shock front structure, which was not clearly resolved in the previous SPH simulations, is clearly captured by the present simulations. Our results confirm that shock heating plays an important role in the heating process of intracluster medium.

1

In addition, we find that a sound wave propagates outward, thereby producing modulations with amplitudes of ~ 10 % in the radial temperature and density profiles which, in turn, causes time variations in the strength of the shock. Such modulations, if observed, could be used as a probe to investigate the internal structure of clusters and the initial temperature of gas.

In part III of this thesis, we investigate evolution of the intracluster medium (ICM), considering the relaxation process between the ions and electrons. According to the standard scenario of structure formation, ICM is heated by the shock in the accretion flow to the gravitational potential well of the dark halo. The shock primarily heats the ions because the kinetic energy of an ion entering the shock is larger than that of an electron by the ratio of masses. Then the electrons and ions exchange the energy through coulomb collisions and reach the equilibrium. From simple order estimation we find that the region where the electron temperature is considerably lower than the ion temperature spreads out on a Mpc scale. We then calculate the ion and electron temperature profiles by combining the adiabatic model of two-temperature plasma by Fox & Loeb (1997) with spherically symmetric N-body and hydrodynamic simulations based on three different cosmological models. It is found that the electron temperature is about a half of the mean temperature at radii ~ 1 Mpc. This could lead to an about 50 % underestimation in the total mass contained within $\sim$ 1 Mpc when the electron temperature profiles are used. The polytropic indices of the electron temperature profiles are $\simeq 1.5$ whereas those of mean temperature $\simeq 1.3$ for $r \geq 1$ Mpc. This result is consistent both with the X-ray observations on electron temperature profiles and with some theoretical and numerical predictions about mean temperature profiles.

The results in Part II have been already reported in Takizawa & Mineshige (1998). The author is responsible for developing the numerical code and the analyses of numerical data. The interpretations of results and the discussions have been made cooperatively between the author and S. Mineshige. The results in Part III have been reported in Takizawa (1998).

ACKNOWLEDGMENT

Contents

Part I
BASIC CONCEPTS

1 GRAVITATIONAL MANY BODY SYSTEMS

In many astronomical systems such as globular clusters, galaxies, and clusters of galaxies etc, gravity plays crucial roles in their dynamical evolution because it is long-ranged force and does not have shielding effect. Thus, these systems can be regard as gravitational many body systems, which consist of particles interacting only through gravitational force and are governed by the equations of motion

$$\frac{d^2 \boldsymbol{r}_i}{dt^2} = -G \sum_{i \neq j}^{N} m_j \frac{\boldsymbol{r}_i - \boldsymbol{r}_j}{|\boldsymbol{r}_i - \boldsymbol{r}_j|^3}, \tag{1}$$

where $\boldsymbol{r}_i$ and m_i are the position and mass of the i-th particle, G is the gravitational constant, and N is the number of particles.

There are two important timescales in gravitational many body systems. One is a crossing timescale t_{cr} and the other is a two-body relaxation timescale t_{rel}.

t_{cr} is the typical timescale where particles across the system (eg., Binney & Tremaine 1987),

$$t_{cr} \sim \frac{1}{\sqrt{G\rho}}, \tag{2}$$

where ρ is the mass density of the system. The system reaches a dynamical equilibrium state within several t_{cr}. In clusters of galaxies, t_{cr} is an order of 10^9 yr, which is about one tenth of the Hubble time ($\sim 10^{10}$ yr).

t_{rel} is the typical timescale where initial information of a particle is washed out through gravitational two-body encounters. There are two kinds of definition in t_{rel}. One is the timescale where a test particle's trajectory is reflected by 90 degrees and the other is that where the fluctuation of a test particle's energy becomes comparable to its energy. Both of them become the same order. From the detailed calculations by Spitzer and Hart (1971),

$$t_{rel} = \frac{v^3}{4\pi G^2 m^2 n \ln(0.4N)}, \tag{3}$$

where v is the root mean square velocity of the system and n is the number density of the system. Using virial theorem, we obtain the relation between t_{cr} and t_{rel}

$$t_{rel} \sim \frac{N}{100} t_{cr}. \tag{4}$$

6

In clusters of galaxies, $t_{\rm rel}$ is longer than Hubble time. Hence, two-body relaxation is negligible there.

Another relaxation process in gravitational many body systems is proposed by Lynden-Bell (1967) to explain the universality of the surface brightness distribution of elliptical galaxies. When there exists coherent motion in the system, gravitational potential of the system (ψ) explicitly depends on the time. Thus, energy per unit mass of a particle (ϵ) changes as

$$\frac{d\epsilon}{dt} = \frac{\partial \psi}{\partial t}.$$ (5)

The relaxation process caused by this process is called "violent relaxation". The relaxation time of violent relaxation is comparable to $t_{\rm cr}$, which is shorter than the two-body relaxation time. When the violent relaxation is ideally effective, it is expected that coarse-grained entropy in the system becomes maximum. Then, the Lynden-Bell distribution is realized in the system and coarse-grained distribution function ($\bar{f}$) becomes

$$\bar{f}(\epsilon) = \eta \frac{\exp\{-\beta(\epsilon - \mu)\}}{1 + \exp\{-\beta(\epsilon - \mu)\}},$$ (6)

where η, β, and μ are the constants. In almost cases of real astronomical systems, we can treat them in the non-degeneracy limit ($\bar{f} \ll \eta$). Thus, we can approximate equation (6) to the Maxwellian, $\bar{f}(\epsilon) \propto \exp(-\beta\epsilon)$. In contrast to the prediction made by Lynden-Bell, numerical simulations have shown that violently relaxed systems do not necessarily reach the Lynden-Bell distribution. The reason is still unclear. Recently, Takizawa, Inagaki, & Hozumi (1999) shows that incompleteness of relaxation due to the damping of coherent motion may be a main factor of this problem.

2 BASIC PHYSICS OF INTRACLUSTER MEDIUM

In ICM, timescale which corresponds to $t_{\rm cr}$ in gravitational many body systems is sound crossing time, $t_{\rm sc}$. ICM temperature is nearly virial one and specific energy ratio of galaxies and ICM is about unity. Thus, $t_{\rm sc}$ is the same order of $t_{\rm cr}$ and becomes $\sim 10^9$ yr.

Since thermal bremsstrahlung is the most dominant radiative process in ICM, radiative cooling timescale $t_{\rm c}$ is

$$t_{\rm c} = 8.5 \times 10^{10}{\rm yr} \left(\frac{n_{\rm e}}{10^{-3}{\rm cm}^{-3}}\right)^{-1} \left(\frac{T_{\rm e}}{10^8{\rm K}}\right)^{1/2},$$ (7)

where $n_{\rm e}$ and $T_{\rm e}$ are the density and temperature of electrons, respectively. This timescale is usually longer than the Hubble time. Therefor, radiative cooling does not plays an

important role in dynamical evolution of the overall cluster structure. However, in the central parts of some clusters, t_c becomes shorter than the Hubble time. In this case, it is possible that cooled gas accretes to the center losing the pressure support, which is called "cooling flow". It is controversial that there really exits cooling flow in the center of clusters of galaxies.

The mean free path of the electrons and ions in a plasma without magnetic field are determined by Coulomb collisions. If we assume that $T_e = T_i$, the mean free path λ is

$$\lambda = 23\text{kpc}\left(\frac{T}{10^8\text{K}}\right)^2\left(\frac{n_e}{10^{-3}\text{cm}^{-3}}\right)^{-1}. \tag{8}$$

This is shorter than a length scale of typical clusters (~ 1 Mpc). Thus we can use hydrodynamic equations to follow evolution of ICM in a cluster scale. However, λ is comparable to the typical size of galaxies. Therefor we should treat ICM as collisionless plasma when we investigate the interaction between ICM and individual galaxies.

The two-body relaxation timescale is determined by $t_{\text{rel}} \equiv \lambda / < v >_{\text{rms}}$, where the denominator is the rms velocity. The timescale for electrons (t_{ee}) is

$$t_{\text{ee}} = 3.3 \times 10^5\text{yr}\left(\frac{T_e}{10^8\text{K}}\right)^{3/2}\left(\frac{n_e}{10^{-3}\text{cm}^{-3}}\right)^{-1}. \tag{9}$$

The timescale for protons is $t_{\text{pp}} \approx (m_p/m_e)^{1/2}t_{\text{ee}}$, or roughly 43 times longer than the value in equation (9). These timescales are usually shorter than both t_{sc} and t_c. Thus we can assume electrons and protons are in thermal equilibrium, respectively. However, the timescale for electrons and ions to reach equipartition becomes comparable to the dynamical timescale. The relaxation time for electrons and ions is

$$t_{\text{ep}} = 2.0 \times 10^8\text{yr}\left(\frac{T_e}{10^8\text{K}}\right)^{3/2}\left(\frac{n_i}{10^{-3}\text{cm}^{-3}}\right)^{-1}. \tag{10}$$

Thus, when we investigate the phenomena in outer low density regions or the temporal events like merger, two-temperature nature of ICM should be considered (Takizawa 1998; Takizawa 1999). We investigate this issue in Part III.

If there exits a gradient in the electron temperature, heat is conducted down the temperature gradient. Thus thermal conduction , if efficient, erases temperature fluctuations on a small scale. The conduction timescale t_{cond} is

$$t_{\text{cond}} = 3 \times 10^7\text{yr}\left(\frac{n_e}{10^{-3}\text{cm}^{-3}}\right)\left(\frac{T_e}{10^8\text{K}}\right)^{-5/2}\left(\frac{l_{\text{T}}}{0.1\text{Mpc}}\right)^2, \tag{11}$$

where, l_{T} is the scale length of temperature gradient.

When there exits magnetic field, charged particles gyrate around magnetic field lines with the gyroradius of $r_{\text{g}} = (mv_\perp/ZeB)$, where $v_\perp$ is the component of the velocity perpendicular

8

to the magnetic field, Z is the particle charge, and B is the magnetic field strength. If $v_\perp = \sqrt{2k_B T/m}$, which is the rms velocity in a thermal plasma, then

$$r_g = \frac{3.1 \times 10^8 \text{cm}}{Z} \left(\frac{T}{10^8 \text{K}}\right)^{1/2} \left(\frac{m}{m_e}\right)^{1/2} \left(\frac{B}{1\mu\text{G}}\right)^{-1}. \tag{12}$$

This value is much smaller than that of λ in equation (8). Thus, the effective mean free path for diffusion perpendicular to the magnetic is only on the order of r_g^2/λ.

3 MASS ESTIMATION OF CLUSTERS OF GALAXIES

Mass estimation of clusters of galaxies is important. Total mass of a cluster of galaxies is one of crucial parameters which represent the physical properties of itself. Furthermore, this is related to some cosmological problems, which are the dark matter problem, determination of baryon fraction, and determination of density parameters, etc. There are three representative methods to determine mass of a cluster of galaxies. These are the hydrostatic method, the galaxy velocity dispersion method, and the gravitational lensing method.

3.1 The Hydrostatic Method

As seen in §2, sound crossing time of ICM in typical clusters is $\sim 10^9$ yr, which is shorter than cluster age. Thus it is not a bad assumption that ICM is in hydrostatic equilibrium. Then we can derive total mass from the X-ray observational data as follows. Density distribution of ICM can be derived from the X-ray surface brightness map and, if possible, temperature distribution also can be obtain from the spatially resolved X-ray spectroscopic data. In this case, the mass is given by the hydrostatic equation, which can be written in spherically symmetric case as

$$M(r) = -\frac{kT(r)r}{\mu m_p G} \left(\frac{d\ln n}{d\ln r} + \frac{d\ln T}{d\ln r}\right), \tag{13}$$

where $M(r)$ is the total mass inside r and μ is the mean molecular weight. Before the launch of ASCA satellite, however, it is difficult to obtain temperature profiles except few clusters with fairly good observational conditions. In this case, emissivity-weighted mean temperature T_{ew} derived from the whole cluster spectroscopic data is used. On the assumption that ICM is isothermal, the mass is

$$M(r) = -\frac{kT_{ew}r}{\mu m_p G} \frac{d\ln n}{d\ln r}. \tag{14}$$

9

Since emissivity is strongly depends on the gas density, T_{ew} becomes close to the temperature in the central high density region. Therefor, deviation from isothermality becomes important in the outer regions of clusters (Takizawa & Mineshige 1998b).

Note that this method relies on the assumption that ICM is in hydrostatic equilibrium through the thermal pressure support. If there exists bulk flow in ICM, mass can be underestimated. This situation corresponds to the cases of merging clusters. If non thermal pressure support is significant, mass also can be underestimated. Possible candidates are magnetic pressure, turbulent, cosmic-ray heating, etc.

3.2   The Galaxy Velocity Dispersion Method

As the case of ICM, galaxies can be regard as in dynamical equilibrium since t_{cr} is shorter than cluster age. Hence, we can estimate cluster mass from the velocity dispersion of member galaxies.

We use the Jeans equation of spherical symmetric case (Binney & Tremaine 1987),

$$\frac{d(\rho \bar{v_r^2})}{dr} + \frac{\rho}{r}\left[2\bar{v_r^2} - (\bar{v_\theta^2} - \bar{v_\phi^2})\right] = -\rho\frac{d\Phi}{dr}, \tag{15}$$

where ρ is the mass density and Φ is the gravitational potential of the system. We assume $\bar{v_\theta^2} = \bar{v_\phi^2}$. We introduce a parameter $\beta(r)$ which describes the degree of anisotropy of the velocity distribution,

$$\beta \equiv 1 - \frac{\bar{v_\theta^2}}{\bar{v_r^2}}. \tag{16}$$

Then, on setting $(d\Phi/dr) = GM(r)/r^2$, we can determine the mass $M(r)$,

$$M(r) = -\frac{r\bar{v_r^2}}{G}\left(\frac{d\ln\rho}{d\ln r} + \frac{d\ln\bar{v_r^2}}{d\ln r} + 2\beta\right). \tag{17}$$

This method, however, is more difficult than the hydrostatic method. In general, measurement of spatially resolved galaxy number density is more difficult that that of X-ray surface brightness. Galaxy number is nearly proportional to density whereas X-ray surface brightness is proportional to the square of density. Thus, galaxy number density is more affected by the background fluctuations. In addition, we does not have any observational information about $\beta(r)$ since it is extremely difficult to measure the transverse component of galaxy motions.

3.3   The Gravitational Lensing Method

Clusters of galaxies are the most massive virialized objects in the universe. Their huge mass concentrations deflect the light from the background objects. Gravitational lensing

10

is the direct method to probe gravitational mass, which does not need any assumptions about dynamical states of clusters. In the gravitational lensing theory, the critical surface mass density Σ_{cr} is a characteristic value which separates strong from weak lensing. This value is

$$\Sigma_{cr} \equiv \frac{c^2}{4\pi G} \frac{D_s}{D_{ls} D_l},$$ (18)

where D_s, D_l, and D_{ls} are the distance between the source and the observer, that between the lens and the observer, and that between the lens and the source, respectively. If the lens and source are cosmological objects, we should use angular-diameter distance.

The simplest situation in which a mass can be determined is that of a spherical lens with a source right behind the lens' center. If the lens is sufficiently strong, the source will form a ring-shaped image, which is called "Einstein ring". In this case, mean surface mass density inside the ring is Σ_{cr}. Thus the mass inside the ring is

$$M(< \theta) = \pi (D_l \theta)^2 \Sigma_{cr},$$ (19)

where θ is the separation angle of the ring from the center. When the cluster has non-axisymmetric structure, however, the situation is more complicated. The determination of mass depends on the modeling of the mass distribution.

When lensing is weak, gravitational potential of a cluster distorts the images of the background galaxies. Kaiser & Squires (1993) develops a non-parametric method to reconstruct the mass distribution from the statistical study of distortions of these images. Complex shear γ (which is defined later through statistical property of background galaxies' images) is related to the normalized surface mass density $\kappa \equiv \Sigma/\Sigma_{cr}$,

$$\gamma(\boldsymbol{\theta}) = \frac{1}{\pi} \int_{\mathbf{R}^2} d^2\theta' \mathcal{D}(\boldsymbol{\theta} - \boldsymbol{\theta}') \kappa(\boldsymbol{\theta}'),$$ (20)

with the complex function

$$\mathcal{D}(\boldsymbol{\theta}) = \frac{\theta_2^2 - \theta_1^2 - 2i\theta_1\theta_2}{|\boldsymbol{\theta}|^4}.$$ (21)

This relation can be inverted by Fourier method, to yield

$$\kappa(\boldsymbol{\theta}) = \frac{1}{\pi} \int_{\mathbf{R}^2} d^2\theta' \mathcal{R}e[\mathcal{D}^*(\boldsymbol{\theta} - \boldsymbol{\theta}')\gamma(\boldsymbol{\theta}')] + \kappa_0,$$ (22)

where the asterisk denotes complex conjugation and $\mathcal{R}e(x)$ is the real part of the complex variable x. Hence, if the tidal field γ can be measured, the surface mass density of the cluster can be obtained up to overall constant. The reason for this constant to occur is that

11

homogeneous mass sheet does not cause any shear. If we assume that intrinsic ellipticity of background galaxies distributes isotropically, mean complex ellipticity $< \epsilon >$ is

$$< \epsilon > = \frac{\gamma}{1 - \kappa}. \tag{23}$$

In linear case ($\kappa \ll 1$), equation (22) is directly solved with $\gamma = < \epsilon >$. In nonlinear case, κ can be solved by the iterative method with equation (22) and (23).

4 THE SELF-SIMILAR MODEL AND THE LUMINOSITY TEMPERATURE RELATION

We introduce a simple model which describe the statistical property of clusters of galaxies, the self-similar model (Kaiser 1986). There are three assumptions in this model.

1. ICM temperature T is equal to virial one,

$$T \sim \frac{GM}{R}, \tag{24}$$

where M and R is total mass and virial radius of a cluster, respectively.

2. Central density of clusters ρ are proportional to the critical density at the formation redshift z_{f},

$$\rho \sim \rho_{\mathrm{cr},0}(1 + z_{\mathrm{f}}), \tag{25}$$

where $\rho_{\mathrm{cr},0}$ is the critical density at the present.

3. Structure of clusters is self-similar,

$$\rho_{\mathrm{ICM}} \sim \rho, \tag{26}$$

where ρ_{ICM} is the density of ICM.

On the other hand, X-ray luminosity $L \sim \rho_{\mathrm{ICM}}^2 R^3 T^{1/2}$ since X-ray emissivity is proportional to $\rho_{\mathrm{ICM}}^2 T^{1/2}$. Thus, T and L depend on only M and $(1 + z_{\mathrm{f}})$,

$$T \quad \sim \quad M^{2/3}(1 + z_{\mathrm{f}}), \tag{27}$$
$$L \quad \sim \quad M^{4/3}(1 + z_{\mathrm{f}})^{7/2}. \tag{28}$$

Using these relations we obtain the luminosity-temperature (LT) relation,

$$L \sim T^2(1 + z_{\mathrm{f}})^{3/2}. \tag{29}$$

12

If we can neglect the variation of z_f, $L \sim T^2$. This relation is not consistent with the X-ray observational results, which suggest $L \sim T^{2.5-3.0}$ (eg; Edge & Stewart 1991; Markevitch 1998; Arnaud & Evrard 1998).

However, it is most likely that z_f depends on M. According to the spherical model for non-linear collapse (see Peebles 1980, Padmanabhan 1993, etc), the relation between z_f and M is associated to the power spectrum of the cosmological density fluctuation field $P(k)$. For simplicity we assume that $P(k)$ obeys power law $P(k) \propto k^n$ and Einstein de Sitter Universe. Then,

$$(1 + z_f) \propto M^{-(n+3)/6}. \tag{30}$$

In this case, LT relation is

$$L \sim T^{(7n+5)/(2n-2)}. \tag{31}$$

The effective index of $P(k)$ of CDM is $-1 \sim -2$ in the galactic and cluster scale, which depends on the shape parameter $\Gamma \equiv \Omega_0 h_0^2$. Thus $L \sim T^{0.5-1.5}$ and the discrepancy becomes larger.

There are several candidates which will be able to solve this discrepancy, which is not considered in the self-similar model. One of these is supernova heating from proto-galaxies. If the heating is substantial, it is expected that the cluster structure is not self-similar. In this case, $\rho_{ICM} \sim f(M)\rho$, where $f(M)$ is an increasing function of M. The reason is as follows. Larger clusters are hardly affected by the heating because the gravitational energy is sufficiently larger than that ejected from proto-galaxies. On the other hand, smaller clusters are significantly affected. Since gas fraction becomes lower than without the heating, luminosity decreases. Therefor, the slope of LT relation can be larger.

5   SUNYAEV-ZEL'DOVICH EFFECT

Since a electron in ICM has much higher energy than a cosmic microwave background (CMB) photon, CMB photons can obtain energy from ICM through an inverse Compton scattering. Hence, the CMB spectrum is distorted in the direction of clusters of galaxies. This is called (thermal) Sunyaev-Zel'dovich (SZ) effect (Sunyaev & Zel'dovich 1972). Since the total number of photons is conserved, the resultant CMB spectrum is not a blackbody one. On the other hand, when clusters have peculiar velocity to the CMB rest frame, CMB spectrum is distorted in a different way. This is called kinematic SZ effect (Sunyaev & Zel'dovich 1980). The discussion here is based on Yoshikawa, Itoh & Suto (1998).

The spectral intensity due to the thermal SZ effect is,

$$\Delta I_\nu = \iota_0 y g(x), \tag{32}$$

13

where $\imath_0 \equiv 2(kT_{\mathrm{CMB}})^3/(hc)^2$, y is the Compton $y-$parameter,

$$y = \int_{-\infty}^{+\infty} \frac{kT_{\mathrm{e}}}{m_{\mathrm{e}}c^2} \sigma_{\mathrm{T}} n_{\mathrm{e}} dl, \tag{33}$$

and $g(x)$ is a function of $x \equiv h\nu/(kT_{\mathrm{CMB}})$,

$$g(x) = \frac{x^4 e^x}{(e^x - 1)^2} \left[x \coth\left(\frac{x}{2}\right) - 4 \right]. \tag{34}$$

Thus, clusters are negative sources in a mm band whereas they are positive sources in a submm band. The corresponding change of the CMB temperature due to the thermal SZ effect is

$$\frac{\Delta T^{\mathrm{th}}}{T_{\mathrm{CMB}}} = y \frac{g(x)}{x^2}. \tag{35}$$

Thus, in the Rayleigh-Jeans limit ($x \ll 1$) it becomes,

$$\frac{\Delta T^{\mathrm{th}}}{T_{\mathrm{CMB}}} = -2y. \tag{36}$$

On the other hand, the spectrum intensity due to the kinematic SZ effect is

$$\Delta I_\nu^{\mathrm{kin}} = -\imath_0 \frac{v_r}{c} \tau h(x), \tag{37}$$

where v_r is the line-of-sight component of the cluster peculiar velocity, τ is the cluster optical depth, and

$$h(x) = \frac{x^4 e^x}{(e^x - 1)^2}. \tag{38}$$

ICM temperature distribution is needed to calculate τ. When ICM is isothermal, $\tau = y \times (m_{\mathrm{e}}c^2)/(kT_{\mathrm{e}})$. Since thermal and kinetic SZ effect have different frequency dependence, multi wavelength observations (eg; mm and submm bands) enable us to distinguish both two effects and estimate a cluster peculiar velocity.

SZ effect brings us information about $n_{\mathrm{e}} T_{\mathrm{e}} R$, where R is radius of a cluster. On the other hand, X-ray surface brightness and X-ray spectrum contain information about $n_{\mathrm{e}}^2 T_{\mathrm{e}}^{1/2} R$ and T_{e}, respectively. Thus, we can estimate R combining these observational results. This fact is used to estimate cosmological parameters (see §6.1).

14

6 COSMOLOGICAL PARAMETERS AND CLUSTERS OF GALAXIES

Clusters of galaxies are the largest virialized objects in the universe and their evolutional timescale is comparable to the cosmic age. Some information about initial cosmological density fluctuation field still remains in them and their evolution is affected by cosmology. In addition, clusters are relatively simple systems and easier to construct evolutional models than galaxies and AGNs. Therefor, there are several trials to estimate cosmological parameters (H_0, Ω_0, λ_0, σ_8, etc) from various properties of clusters. We introduce some of these trials.

6.1 Cosmological Parameters from the SZ Effect

As described in §5, we can estimate a cluster radius using results of both X-ray and SZ effect observations. Then we can estimate the angular-diameter distance of the cluster from its viewing angle. If we know the redshift of the cluster, we can obtain a series of cosmological parameters (H_0, Ω_0, λ_0). This is the essence of this section.

To calculate in more detail, models of ICM density and temperature distribution is needed. We adopt isothermal $\beta-$model:

$$n_e(r) = n_{e0}\left[1+\left(\frac{r}{r_c}\right)^2\right]^{-3\beta/2}, \tag{39}$$

$$T_e(r) = T_{e0}. \tag{40}$$

Then the X-ray surface brightness is

$$S_x(\theta) = \frac{\alpha(T_e)n_{e0}^2 r_c}{4\sqrt{\pi}(1+z)^4}\frac{\Gamma(3\beta - 1/2)}{\Gamma(3\beta)}\left[1+\left(\frac{d_A\theta}{r_c}\right)^2\right]^{-3\beta+1/2}, \tag{41}$$

where $\alpha(T_e)$ is the cooling function and d_A is the angular-diameter distance, which is in the limit of $z \ll 1$

$$d_A \simeq \frac{cz}{H_0}\left[1 + \frac{2\lambda_0 - \Omega_0 - 6}{4}z + O(z^2)\right]. \tag{42}$$

We consider only thermal SZ effect. Then temperature decrement of Rayleigh-Jeans region is

$$\frac{\Delta T}{T_{CMB}}(\theta) = -\frac{2\sqrt{\pi}\sigma_T k T_e}{m_e c^2}n_{e0}r_c\frac{\Gamma(3\beta/2 - 1/2)}{\Gamma(3\beta/2)}\left[1+\left(\frac{d_A\theta}{r_c}\right)^2\right]^{-3\beta/2+1/2}. \tag{43}$$

From equation (41) and (43) we find

$$r_c = \frac{(\Delta T(\theta)/T_{CMB})^2}{S_X(\theta)}\frac{\Gamma(3\beta - 1/2)\Gamma(3\beta/2)^2}{\Gamma(3\beta)\Gamma(3\beta/2 - 1/2)^2}\frac{m_e c^4\alpha(T_e)}{16\pi^{3/2}(1+z)^4\sigma_T^2 k^2 T_e^2}[1 + (\theta/\theta_c)^2]^{-1/2}, \tag{44}$$

15

where θ_c is the angular radius of the core observed by X-ray imaging. Then we find the angular-diameter distance of the cluster $d_A(z) = \theta_c/r_c$. Using equation (42) we can determine the series of parameters.

6.2 Cluster Abundance and Cosmological Parameters

Observational statistical results of clusters of galaxies such as temperature function, luminosity function, $\log N - \log S$ relation etc, contain information about the initial density fluctuation field and cosmology. We can determine some cosmological parameters comparing these observations with theoretical models or results of cosmological numerical simulations.

To construct such a model to describe cluster statistical property, Press-Schechter mass function is often used (Press & Schechter 1974). Kitayama & Suto (1997) compare their theoretical model of $\log N - \log S$ relation to the results of ROSAT Deep Cluster Survey and ROSAT Brightest Cluster Sample. Their results especially constrain the relation between σ_8 and Ω_0. They find a fitting formula of the relation when $h_0 = 0.7$. For flat universe $(\Omega_0 + \lambda_0 = 1)$,

$$\sigma_8 = (0.54 \pm 0.02) \times \Omega_0^{-0.35 - 0.82\Omega_0 + 0.55\Omega_0^2}. \tag{45}$$

When $\lambda_0 = 0$,

$$\sigma_8 = (0.54 \pm 0.02) \times \Omega_0^{-0.28 - 0.91\Omega_0 + 0.68\Omega_0^2}. \tag{46}$$

Combining their results and COBE 4 year data, they conclude $(\Omega_0, \lambda_0, h_0, \sigma_8) \simeq (0.3, 0.7, 0.7, 1)$ or $(0.45, 0, 0.7, 0.8)$ is preferable.

6.3 Substructure and Ω_0

According to the hierarchical clustering scenario, it is believed that clusters are formed through subcluster mergers and/or absorptions of smaller galaxy groups. Since in a higher density universe clusters form at a later epoch, the rate of existence of substructure at the present is depend on the Ω_0. Indeed, the rate is an increasing function of Ω_0. Richstone, Loeb, & Turner (1992) estimated this rate analytically and compared some observational results. Their conclusion is that Ω_0 is greater than ~ 0.5.

However, the estimation of Ω_0 through this method is sensitive to the timescale of mergers. Underestimation of merging timescale leads to the overestimation of Ω_0 (Nakamura, Hattori, & Mineshige 1995). Indeed, cosmological N-body simulations of Jing et al. (1995) also suggests low Ω ($\simeq 0.3$) universe.

16

6.4 Baryon Fraction and Ω_0

Clusters of galaxies have two baryonic components; galaxies and ICM. Mass of galaxies (M_{gal}) can be measured from their luminosity on a proper assumption of mass to light ratio. ICM mass (M_{ICM}) also can be estimated from their X-ray luminosity. Thus we can determine baryonic mass in a cluster combining these two results. On the other hand, total mass of a cluster (M_{tot}) is determined through the methods described in §3. In this way we can measure baryonic fraction f_{b} in a cluster

$$f_{\mathrm{b}} = \frac{M_{\mathrm{gal}} + M_{\mathrm{ICM}}}{M_{\mathrm{tot}}}. \tag{47}$$

Typically $f_{\mathrm{b}} \sim 0.1$ since $M_{\mathrm{gal}} : M_{\mathrm{ICM}} : M_{\mathrm{tot}}$ becomes $0.1 \sim 1 : 1 :\sim 10$.

If we assume that the cluster's baryon fraction is equal to that of the universe, we can determine Ω_0,

$$\Omega_0 = \frac{\Omega_{\mathrm{b}}}{f_{\mathrm{b}}}. \tag{48}$$

According to the primordial nucleo synthesis theory, $\Omega_{\mathrm{b}} \simeq 0.012h^{-2}$ (Walker et al. 1991). Thus, typically $\Omega_0 \sim 0.1h^{-2}$.

However, the assumption of the universality of the baryon fraction among the universe and individual clusters is rather problematic. As discussed in §4, it is most likely that the baryon fraction of clusters depends on cluster mass. If radiative cooling is effective and supernova heating is not significant in the cluster center, baryon fraction of clusters becomes greater than that of the universe (Suginohara & Ostriker 1998).

Part II
DYNAMICAL EVOLUTION OF ICM

7 INTRODUCTION

Clusters of galaxies (CG) are the largest virialized objects in the universe, which contain collisionless particles, galaxies and dark matter, and a diffuse gas component. The gas component is called intracluster medium (ICM). The ICM is the plasma with temperature of about 10^8 K, thus emitting X-ray mainly through the thermal bremsstrahlung of the electrons (Sarazin 1988).

Recent X-ray and optical observations have revealed dynamical aspects of CGs (Fabricant, Kent, & Kurtz 1989; Kneib et al. 1995). On the other hand, recent relatively deep observations suggest lack of significant evolution at $z \sim 0.3$ in the X-ray luminosity function (Burke et al. 1997; Collins et al. 1997; Ebeling et al. 1997; Rosati et al. 1998), in the iron abundance (Mushotzky & Loewenstein 1997), and in the luminosity-temperature relation (Mushotzky & Scharf 1997). To understand the structural evolution of CGs, therefore, it is essential to examine the details of the non-equilibrium processes.

Recent extensive X-ray observations have established that the radial temperature profiles of ICM are nearly flat in many clusters (Fabian 1994; Ohashi et al 1997). Although there is no widely accepted explanation for this, it is, at least, certain that shock heating through gravitational collapse should play an important role there. It then follows that the isothermality of gas may reflect the shape and time evolution of the gravitational potential well. The effect of shock heating also can explain the luminosity-temperature relation for groups and clusters of galaxies (Cavaliere, Menci, & Tozzi 1997). What then governs the total dynamics of CGs? Obviously galaxies and dark matter (DM) are most important, and both of them can be treated as a collisionless self-gravitating particles. Dynamics of the ICM, a collisional fluid on a CG scale, simply follows the dynamical evolution of the gravitational potential mainly contributed by DM and galaxies. Thus, the thermal history of the ICM is rather sensitive to such violent time variation of gravitational potential field as occur in cluster formation, merger, etc. Violent relaxation (Lynden-Bell 1967) is thought to play a crucial role there, although its physical basis is still poorly understood in detail (Funato, Makino, & Ebisuzaki 1992a,b; Takizawa, Inagaki, & Hozumi 1999).

CGs are believed to be formed by gravitational collapse of overdense perturbations in the universe. After being decoupled from the cosmological expansion they grew through gravitational instability and collapsed at $z \sim 1$. CGs are still growing further at the present by accreting ambient matter. Gunn & Gott (1972) discussed analytically the

growth of a spherical symmetric perturbation only consisting of collisionless particles in an expanding universe. Bertschinger (1985) found the self-similar solution describing evolution of a spherical density fluctuation consisting of DM and gas in the Einstein-de Sitter universe (where the cosmological density parameter is $\Omega_0 = 1$ and the cosmological constant is $\lambda_0 = 0$).

There have been plenty of numerical studies performed so far regarding the formation and evolution of CGs by using N-body and hydrodynamic codes. Perrenod (1978) was the first to calculate the evolution of a spherical symmetric cluster with standard mesh hydrodynamic code. Some calculations are especially focused on merger events (Schindler & Müller 1993; Ishizaka & Mineshige 1996; Roettiger, Loken, & Burns 1997; Roettiger, Stone, & Mushotzky 1997). Three-dimensional calculations with cosmological initial conditions have been carried out recently, which mostly use smooth particle hydrodynamics (SPH) codes (Evrard 1990; Thomas & Couchman 1992; Bryan et al. 1994; Metzler & Evrard 1994; Navarro, Frenk, & White 1995, hereafter NFW; Eke, Navarro, & Frenk 1997). According to Evrard (1990), a shock front moved outward when gas around the cluster accreted onto the cluster center and a relatively flat temperature profile was realized within the shock front. This result was significant in the sense that the above expectation was confirmed qualitatively. However, quantitative estimation may be problematic because of limited spatial resolutions and poor reliability of SPH code in calculations of shocks. It might be kept in mind that although the SPH codes are easy to work with and could give reasonable accuracy, they are not better for problems with discontinuities (such as strong shock and contact discontinuity) than mesh codes (Monaghan 1992).

Numerical simulations of cosmological structure formation by using N-body and hydro-dynamic mesh code have also been carried out, but on a larger scale mainly to investigate the statistical properties of CGs (Cen & Ostriker 1994; Kang et al. 1994; Anninos & Norman 1996; Pen 1996).

In part II of this thesis, we focus on the dynamical aspects of ICM, such as time-dependent properties of shock waves, the effects of shock heating on the evolution of CGs and other associated phenomena (Takizawa & Mineshige 1998a).

For this purpose, we perform numerical simulations of spherically symmetric CGs with the N-body code based on the shell model and the TVD mesh code. Note that the TVD code is one of the most useful tools to deal with spatial discontinuities. Since we assume spherical symmetry, the problem can be reduced to one-dimensional. Better spatial resolutions can be achieved, therefore. Since the shock formed between $z = 1$ and 2 at about $r = 0.1 - 0.01$ Mpc, the resolution of at least 0.005 Mpc at $z = 0$ is required for following the evolution of gas during the appearance of the shock. Indeed, 3-D calculation by Pen (1996) achieved a good resolution of ~ 0.02 Mpc using the technique of 3-D adaptive mesh, but still this is not sufficient to clearly resolve the shock fronts, and such a high resolution is achieved only in a limited region. Such limited resolutions may have no practical problem for cosmological statistical studies of CGs, but have difficulty in resolving the dynamics of

19

individual CGs.

The reality includes both asymmetric merging of comparable clumps, and more symmetric accretion of smaller lumps, down to nearly spherical infall of almost diffuse gas. So both extreme cases ought to be developed and researched in full. We thus conclude that before performing complex 3-D simulations it is useful to make a careful a 1-D study to clarify basic physics involved with a collapse of proto-cluster fluctuation. Indeed we are concerned with the formation and evolution of individual clusters. Treating the full statics of the L-T relation and of the cosmologically evolving luminosity function is beyond the scope of our paper.

Using the 1-D codes, we calculate dynamical evolutions of a density perturbation of $10^{15} M_\odot$ consisting of DM and gas and collapsing at $z \sim 1$ in the universe with $\Omega_0 = 1$ or 0.2. It is also interesting to investigate how different cosmological models affect evolution of CGs.

Part II of this thesis is organized as follows. In section 8 we describe the adopted numerical methods and the initial conditions. In section 9 we present our results, discussing physical processes underlying the structural evolution of calculated CGs. In section 10 we summarize our results and discuss their implications.

8   THE SIMULATIONS

In the present study we regard the CG consisting of two components: collisionless particles corresponding to galaxies and DM, and gas corresponding to ICM. When calculating gravity both components are considered, although the former dominates over the latter. We also assume spherical symmetry in all our calculations.

8.1   Basic Equations for Collisionless Particles

For calculating the evolution of the collisionless particles we adopt the shell model (Hénon 1964). The distribution function of spherical symmetric stellar systems can be expressed as $f(r, u, v, t)$, where r is radial distance, u is radial velocity, v is tangential velocity, and t is time, respectively. Therefore one state of the system is represented by N points in the (r, u, v) space (N is the number of shells. We set $N = 5000$.) and a trajectory of the i-th point at (r_i, u_i, v_i) is calculated according to the equations of motion;

$$\frac{dr_i}{dt} = u_i, \tag{49}$$

$$\frac{du_i}{dt} = \frac{A_i^2}{r_i^3} - \frac{GM_i}{r_i^2}, \tag{50}$$

for $i = 1 \sim N$, where G is the gravitational constant, $A_i \equiv r_i v_i$ (= constant in time) is angular momentum of the i-th shell, and M_i is the total mass (including the mass of gas)

interior to r_i, respectively. Since it is convenient to carry out numerical calculations using the comoving coordinates for our purpose, we transform (r_i, u_i, v_i) to (R_i, U_i, v_i) as follows;

$$r_i = a(t)R_i, \tag{51}$$

$$u_i = \dot{a}R_i + U_i, \tag{52}$$

where $a(t)$ is the dimensionless scale factor of the universe and $\dot{a}$ represents the derivative of $a(t)$ with respect to time. Equations (49) and (50) are then transformed into

$$\frac{dR_i}{dt} = \frac{U_i}{a}, \tag{53}$$

$$\frac{dU_i}{dt} = \frac{A_i^2}{(aR_i)^3} - \frac{GM_i}{(aR_i)^2} - \frac{\dot{a}}{a}U_i - \ddot{a}R_i, \tag{54}$$

respectively, by using equations (51) and (52). Equations (53) and (54) are integrated by using leap-frog method. As to the inner boundary condition we set a reflecting wall at $r_{\mathrm{rw}} = 0.005/(1 + z)$ with z being a redshift $[1 + z = a(0)/a(t)]$ and impose the condition that when a shell reaches the wall, $r_i < r_{\mathrm{rw}}$, the shell is elastically reflected. Note, however, that only a few shells with rather small angular momentum are influenced by the wall.

8.2 Basic Equations for Gas

For the gas components the basic equations in the comoving frame are

$$\frac{\partial \rho}{\partial t} + \frac{1}{a}\frac{\partial}{\partial R}(\rho v_{\mathrm{gas}}) = -3\frac{\dot{a}}{a}\rho - \frac{2}{aR}\rho v_{\mathrm{gas}}, \tag{55}$$

$$\frac{\partial}{\partial t}(\rho v_{\mathrm{gas}}) + \frac{1}{a}\frac{\partial}{\partial R}(\rho v_{\mathrm{gas}}^2 + P) = -4\frac{\dot{a}}{a}\rho v_{\mathrm{gas}} - 2\frac{\rho v_{\mathrm{gas}}^2}{aR} + \rho g_R, \tag{56}$$

$$\frac{\partial}{\partial t}(\rho E) + \frac{1}{a}\frac{\partial}{\partial R}(\rho H v_{\mathrm{gas}}) = -\frac{\dot{a}}{a}\left(\frac{5}{2}\rho v_{\mathrm{gas}}^2 - \frac{3\gamma}{\gamma-1}P\right) - 2\frac{\rho H v_{\mathrm{gas}}}{aR} + \rho g_R v_{\mathrm{gas}}, \tag{57}$$

where ρ is gas density, v_{gas} is radial velocity of gas, P is gas pressure, and γ is the adiabatic exponent, respectively. The total energy of gas per unit mass, E, and the enthalpy per unit mass, H, are given by

$$E = \frac{P}{\rho(\gamma-1)} + \frac{v_{\mathrm{gas}}^2}{2}, \tag{58}$$

$$H = \frac{\gamma}{\gamma-1}\frac{P}{\rho} + \frac{v_{\mathrm{gas}}^2}{2}, \tag{59}$$

respectively, and g_R is defined by

$$g_R \equiv -\frac{GM_R}{(aR)^2} - \ddot{a}R, \tag{60}$$

21

where, M_R is the total mass (including gas and collisionless particles) inside R.

We neglect viscosity and angular momentum of gas. We also assume that gas is ideal gas with $\gamma = 5/3$. A second order up-wind TVD code (minmod limiter) is used for our simulations (Hirsch 1990). One mesh spacing corresponds to $\triangle r = 0.005/(1+z)$ Mpc. Such a high resolution is necessary to clearly resolve the evolution of gas during the appearance of the shock in the central region of CG at $z \sim 1-2$. This is still sufficiently longer than the mean free path there ($10^{-4} - 10^{-5}$ Mpc). As to the boundary conditions, the inner edge is assumed to be a perfectly reflecting point;

$$\rho_{-1} = \rho_0 = \rho_1, \tag{61}$$

$$P_{-1} = P_0 = P_1, \tag{62}$$

$$v_{\mathrm{gas},-1} = v_{\mathrm{gas},0} = 0, \tag{63}$$

where ρ_i, P_i and $v_{\mathrm{gas},i}$ are gas density, gas pressure, and the radial velocity of gas at the i-th mesh point, respectively, and the first mesh point corresponds to the inner boundary ($r_1 = r_{\mathrm{rw}}$). The 0-th and -1-st points have been introduced for the calculation purpose (i.e, to derive spatial derivatives of physical quantities near the origin). The outer edge is assumed to be a perfectly transmitting surface;

$$q_{n+2} = 3q_n - 2q_{n-1}, \tag{64}$$

$$q_{n+1} = 2q_n - q_{n-1}, \tag{65}$$

where q_i is any physical quantity of gas at the i-th mesh point and the n-th corresponds to the outer boundary. Again, the $(n+1)$-th and $(n+2)$-th points are necessary for the calculation purpose.

8.3 Models and Initial Conditions

In this paper, all the calculations are carried out from $z_{\mathrm{ini}} = 10$ to the present time ($z_0 = 0$). We adopt cosmological models with no cosmological constant, $\lambda_0 = 0$. When $\Omega_0 = 1$, therefore, we find

$$a(t) = \left(\frac{t}{\frac{2}{3}H_0^{-1}}\right)^{\frac{2}{3}}, \tag{66}$$

while when $0 < \Omega_0 < 1$ we have

$$a(t) = \frac{\Omega_0}{2(1-\Omega_0)}(\cosh\psi - 1), \tag{67}$$

$$H_0 t = \frac{\Omega_0}{2(1-\Omega_0)^{3/2}}(\sinh\psi - \psi), \tag{68}$$

22

where H_0 is the Hubble constant and is set to be $H_0 = 100$ (km s^{-1} Mpc^{-1}) in transformations of length and time.

We make initial density profiles in the same manner as Peebles (1982). At first we prepare N concentric shells with a constant density which is taken to be the mean density ($\bar{\rho}$) of the universe at $z_{\mathrm{ini}} = 10$. Then a density fluctuation is introduced by perturbing the radius and velocity of each shell following

$$r_i = r_i^{(0)} \left[1 + \delta(r_i^{(0)}) \right], \tag{69}$$

$$u_i = H(z_{\mathrm{ini}}) r_i^{(0)} \left[1 + 2\delta(r_i^{(0)}) \right], \tag{70}$$

where $r_i^{(0)}$ is the unperturbed coordinate, $\delta(r)$ represents the perturbation as a function of r (specified below), $H(z_{\mathrm{ini}})$ is the Hubble constant at the initial epoch, and we used Zel'dovich approximation and $\delta \propto t^{2/3}$; the relation which holds exactly in the Einstein-de Sitter universe. The functional form of the perturbation is assumed to be

$$\delta(r) = \begin{cases} -\frac{\delta_0}{3} \cos^2(\frac{\pi}{2}\frac{r}{r_0}) & (0 \leq r \leq r_0) \\ 0 & (r_0 < r) \end{cases}, \tag{71}$$

where r_0 and δ_0, respectively, represent the initial size of the fluctuation on the comoving scale and the magnitude of the perturbation (see Nakamura 1996). We take $(\delta_0, r_0) = (0.4, 9.0 \text{ Mpc})$ for Model A (with $\Omega_0 = 1.0$) and $(\delta_0, r_0) = (0.5, 15.4 \text{ Mpc})$ for Model B (with $\Omega_0 = 0.2$), respectively. In both models the fluctuation contains a mass of about $10^{15} M_\odot$ and correspond to typical density peaks with $\sim 1.5\sigma$ in the CDM power spectrum with $\sigma_8 = 0.96$. Here, σ is the rms density fluctuations on a cluster scale and σ_8 is the rms of mass fluctuation on a scale of 8 Mpc; $\sigma_8 = 0.96$ was obtained from the observation of the nearby galaxy distribution (see Suto 1993). The profile of the initial density perturbation and the ratio of $(\delta M/M)/\sigma_{8,\mathrm{CDM}}$ are illustrated in figure 1 for Model A (by the solid line) and B (by the dotted line), respectively. Here, $(\delta M/M)$ is the mass fluctuation averaged over a scale r, whereas $\sigma_{8,\mathrm{CDM}}$ is the rms of mass fluctuation averaged over a scale r obtained from the CDM power spectrum with $\sigma_8 = 0.96$.

The initial conditions of gas are set as follows. At first gas density was everywhere set to be 1/10 of the mean density ($\bar{\rho}$) of the universe at $z = 10$ and temperature of gas ($T_{\mathrm{gas,i}}$) was everywhere taken to be constant; $T_{\mathrm{gas,i}} = 10^7$ K in Model A and B, 10^6 K in Model LT, 10^8 K in Model H1 and 10^9 K in Model H2. We then put adiabatic fluctuation so that the gas density should always be 1/10 of that of DM. Note that after the perturbation is added gas temperature distribution becomes nonuniform, accordingly. We calculated 5 models in total. Model parameters are listed in table 1.
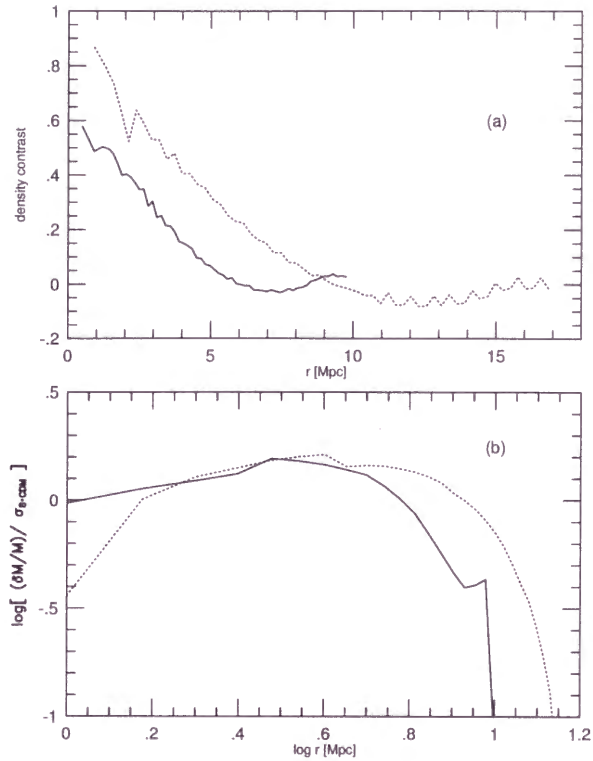
Figure 1: (a) Radial profiles of initial density perturbations and (b) $(\delta M/M)/\sigma_{8,\mathrm{CDM}}$, where $(\delta M/M)$ is the mass fluctuation averaged over a scale r and $\sigma_{8,\mathrm{CDM}}$ is the rms of mass fluctuation of scale r obtained from CDM power spectrum with σ_8 being a normalization. The solid line correspond to Model A and the dotted line corresponds Model B.

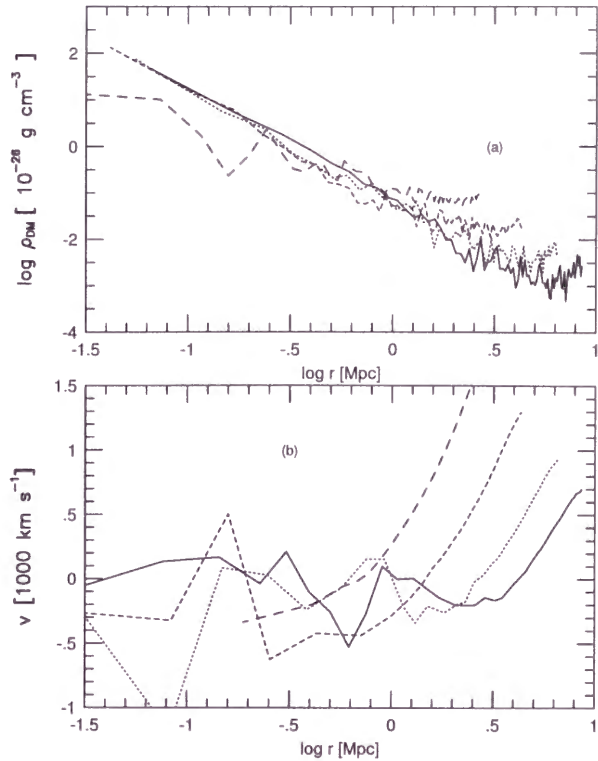| Model	δ_0	r_0 (Mpc)	$T_{\mathrm{gas,i}}$ (K)	Ω_0
A	0.4	9.0	10^7	1.0
B	0.5	15.4	10^7	0.2
LT	0.4	9.0	10^6	1.0
H1	0.4	9.0	10^8	1.0
H2	0.4	9.0	10^9	1.0

Table 1: Parameters of each model.

Figure 2: The evolution of (a) density profile and (b) radial velocity profile of DM of Model A cluster. The different lines correspond to different redshifts (and different times): $z = 2.5$ ($t = 1$ Gyr) by the long dash line; $z = 1.2$ ($t = 2$ Gyr) by the short dash line; $z = 0.4$ ($t = 4$ Gyr) by the dotted line; and $z = 0$ ($t = 6.5$ Gyr) by the solid line, respectively.

9 RESULTS

9.1 Overview of Evolution

At first we overview the evolution of Model A cluster. The evolution of density and radial velocity profiles of the DM component is displayed in figure 2. The different types of lines correspond to different redshifts (and different times): $z = 2.5$ ($t = 1$ Gyr) by the long dash line; $z = 1.2$ ($t = 2$ Gyr) by the short dash line; $z = 0.4$ ($t = 4$ Gyr) by the dotted line; and $z = 0$ ($t = 6.5$ Gyr) by the solid line, respectively.

The Density profile basically obeys a power law, $\rho_{DM} \propto r^{-2.6}$, as expected (Bertschinger 1985). The entire distribution evolves in a self-similar fashion after $z \simeq 1$. The evolutions in the radial distributions of radial velocity, density, temperature, pressure, and entropy (each of the gas component) are summarized in figure 3. The different types of lines correspond to same redshifts as in figure 2.
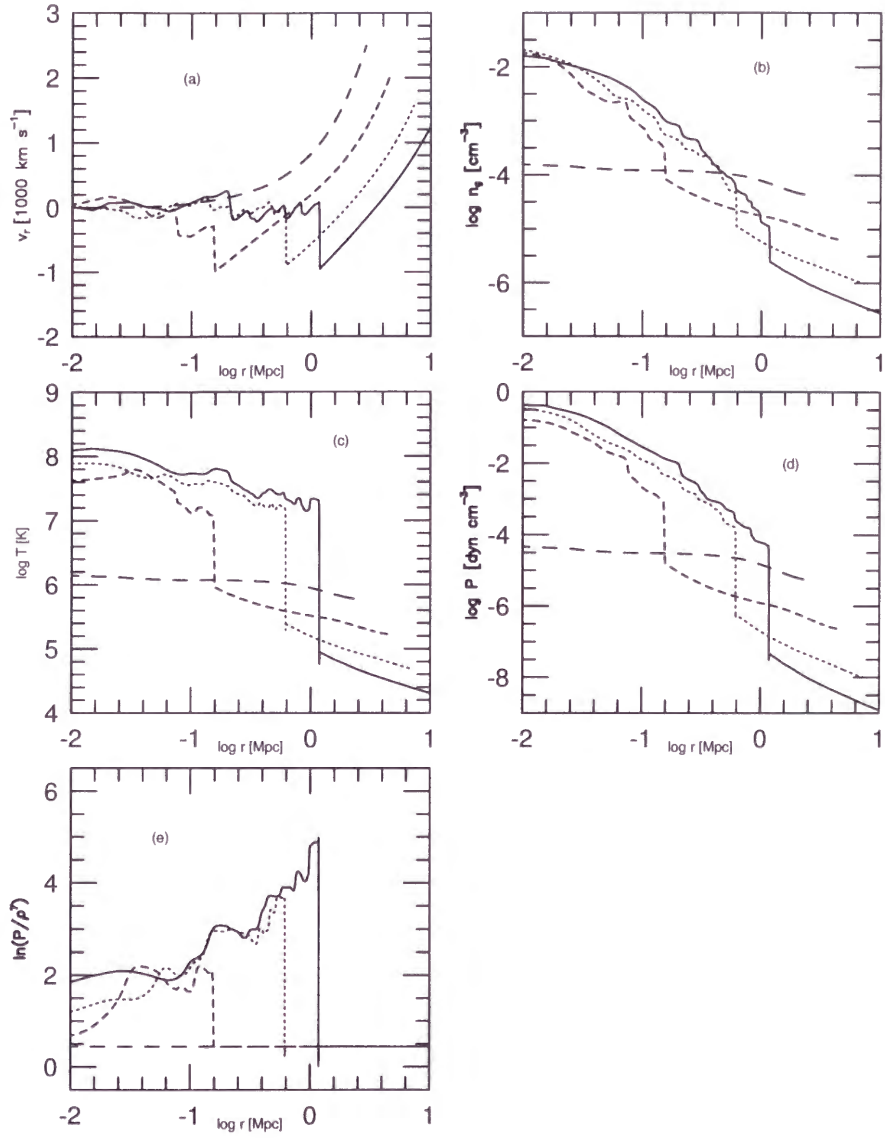
25

Figure 3: Evolution of Model A cluster. Radial profiles of representative physical quantities of gas are showed: (a) radial velocity, (b) density, (c) temperature, (d) pressure, and (e) entropy. The different types of lines correspond to same redshifts as in figure 2

26

There are fundamental features commonly seen in all the models except Model H2, which can be summarized as follows.

1. Before the initiation of DM collapse (at $z \geq 2.5$; $t \leq 1$ Gyr) gas continues to expand, following the cosmological expansion. When DM begins to collapse, a shock wave forms for the gas component in the central part and moves outwards, accreting ambient gas towards the center.

2. The shock front separates the inner hot region from the outer cool region. In the inner region, gas is almost in hydrostatic equilibrium, although bulk velocity of radial infall of ~ 100 km s^{-1} still remains. The temperature profile is relatively flat and gas is hot enough to emit X-ray. In the outer region, in contrast, gas falls almost freely and is too cool to emit X-ray.

3. The Density profile of gas (n_{gas}) evolves self-similarly; $n_{\mathrm{gas}} \propto r^{-2.4}$ inside the shock front except near the center, where density profile is rather flat. Even after the passage of the shock, density, temperature, and, therefore, pressure gradually increase with time. This indicates that the inner region is not perfectly in hydrostatic equilibrium (will be discussed in subsection 9.4).

4. Entropy profile shows an overall increase outwards, suggesting larger entropy production taking place as the shock moves outward. There are wavy features seen, especially, in the distributions of temperature and entropy. These seem to be related to sound wave propagation (will be discussed in subsection 9.4).

In Model H2 the shock does not form because the temperature of infalling gas is higher than virial temperature. Therefore its evolutional behavior and structure are rather different from other models (will be discussed in subsection 9.8).

Let us next examine each item in more details and discuss similarities and differences between different models.

9.2   The Density Profiles

The density profiles of DM at $z = 0$ can well be fitted with the β-model except Model H1;

$$\rho_{\mathrm{DM}}(r) = \rho_{\mathrm{DM},0} \left[1 + \left(\frac{r}{r_{\mathrm{DM}}} \right)^2 \right]^{-3\beta_{\mathrm{DM}}/2}. \tag{72}$$

Here, $\rho_{\mathrm{DM},0}$, r_{DM} and β_{DM} are fitting parameters. We fit the results of simulations inside the radius of r_{200}, where the mean interior density within this radius is 200 times of the critical density at $z = 0$. The results of the fitting are summarized in table 2. The density profile of DM in Model H1 dose not have a core structure so we cannot well determine r_{DM}

Model	$\rho_{\mathrm{DM},0}$ $(10^{-26}$ g cm$^{-3})$	r_{DM} (Mpc)	β_{DM}	r_{200} (Mpc)
A	144.5	0.056	0.88	0.972
B	28.3	0.086	0.88	0.777
LT	109.8	0.064	0.89	0.983
H1	——	——	0.76	0.958
H2	770.7	0.0192	0.77	0.967

Table 2: Density profiles of DM at $z = 0$.

Model	$n_{\mathrm{gas},0}$ $(10^{-3}$cm$^{-3})$	r_{gas} (Mpc)	β_{gas}
A	10.9	0.068	0.81
B	7.78	0.075	0.79
LT	25.2	0.063	0.86
H1	1.13	0.101	0.73
H2	0.117	0.111	0.38

Table 3: Density profiles of gas at $z = 0$.

and β_{DM}. We thus fit the results of Model H1 by the form of $\rho_{\mathrm{DM}} \propto r^{-3\beta_{\mathrm{DM}}}$. Note that these results may slightly depend on initial density profiles.

In the same way density profiles of gas at $z = 0$ inside the shock front can be fitted with the β-model,

$$n_{\mathrm{gas}}(r) = n_{\mathrm{gas},0}\left[1+\left(\frac{r}{r_{\mathrm{gas}}}\right)^2\right]^{-3\beta_{\mathrm{gas}}/2}, \tag{73}$$

where $n_{\mathrm{gas},0}$, r_{gas} and β_{gas} are fitting parameters. In Model H2 the profile is fitted inside the radius of r_{200} instead of the shock front. The results are listed in table 3. In all the calculated models except Model H2 we find $\beta_{\mathrm{DM}} \approx \beta_{\mathrm{gas}} \sim 0.8 - 0.9$ and $r_{\mathrm{DM}} \approx r_{\mathrm{gas}} \sim 0.06 - 0.08$ Mpc. In Model H2, β_{gas} is rather smaller than others.

We also show the nondimensional density profiles at $z = 0$ in figure 4 for Model A (by the solid line) and Model B (by the dotted line), respectively, where density is scaled with ρ_{c0}, critical density of the universe at $z = 0$, and radius is scaled with r_{200}. The nondimensional DM density profiles look similar among two models, whereas the gas component expands slightly in Model B, compared with in Model A.

It is possible that gas density profiles in the central region is influenced by the mesh size. To assess this resolution effect we calculate additional three models which have the
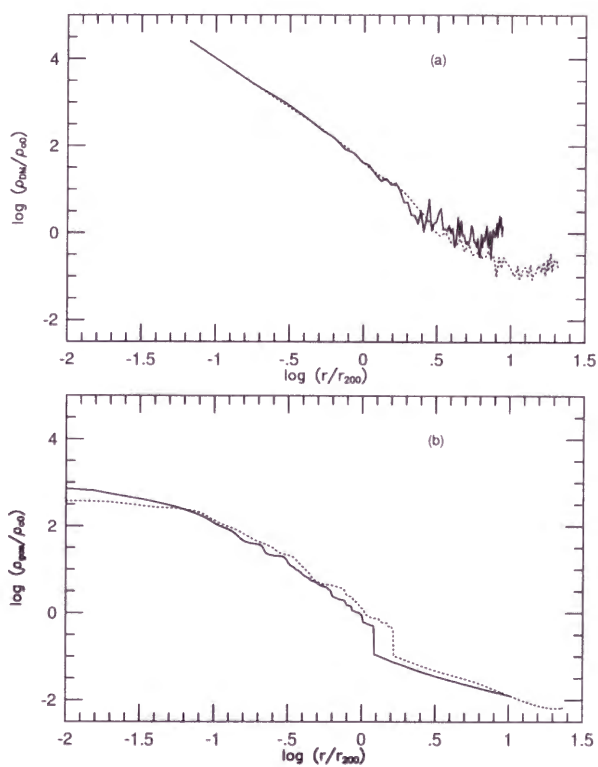
Figure 4: Nondimensional density profiles at $z = 0$ for Models A (by the solid line) and for B (by the dotted line), respectively. Here, density is scaled with ρ_{c0}, critical density of the universe at $z = 0$, and radius is scaled with r_{200}.
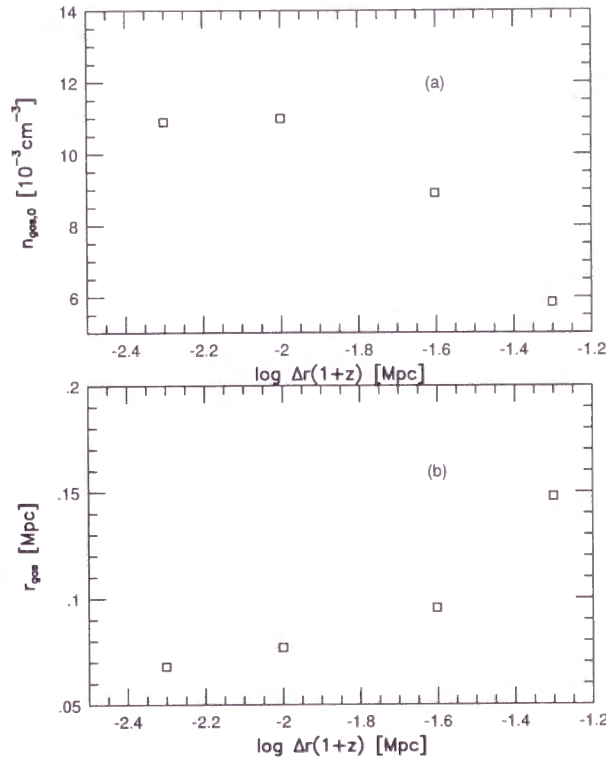
Figure 5: The dependence of $n_{gas,0}$ and r_{gas} on the mesh size in the models which have the same initial condition and cosmological model as in Model A. Both $n_{gas,0}$ and r_{gas} are not sensitive to the resolution when $\Delta < 0.01/(1+z)$ Mpc. Therefore gas density profiles in the central region is well resolved.

same initial condition and cosmological model as those in the Model A but have different mesh sizes: one with doubled mesh size $[\Delta r = 0.01/(1+z)$ Mpc], one with five times larger mesh size $[\Delta r = 0.025/(1+z)$ Mpc], and the other with ten times larger mesh size $[\Delta r = 0.05/(1+z)$ Mpc], respectively. The dependence of $n_{gas,0}$ and r_{gas} on the mesh size is shown in figure 5. Both $n_{gas,0}$ and r_{gas} are not sensitive to the resolution as long as $\Delta r < 0.01/(1+z)$ Mpc. Therefore, gas density profiles in the central region is well resolved. We also note that the calculations with $\Delta r > 0.05/(1+z)$ are bound to overestimate the core radius and underestimation of the central density.

Let us finally compare our results with the previous results (NFW). As for the density profiles of the clusters in the Einstein-de Sitter Universe (Models A and LT), the core radii are somewhat smaller than those of NFW (who obtained $r_{DM} \sim r_{gas} \sim 0.2$), while β_{DM} and β_{gas} are similar. On the other hand, the central DM density, $\rho_{DM,0}$, is similar to that of NFW, whereas the central gas density, $\rho_{gas,0}$, of Model A is lower than that of NFW (our Model LT is consistent with their model; $n_{gas,0} \sim 5 \times 10^{-2}$). This can be explained in

30

terms of different initial gas temperatures (see section 9.8).

9.3 The Temperature Profiles

The Temperature and entropy profiles are shown in figure 6 in the upper and lower panels, respectively. The different types of lines correspond to different models: Model A by the solid line; Model B by the dotted line; Model LT by the short dash line; Model H1 by the long dash line; and Model H2 by the dot-short dash line, respectively. There are common features except for Model H2 as follows. Temperatures gradually fall outwards inside the shock radius, r_{shock}. There are small temperature fluctuations seen. The evaluated propagation speed of fluctuation pattern is ~ 700 km s^{-1}, of the order of the sound speed inside the shock. In addition, the entropy pattern does not change much with the time, indicating that the structural variation is adiabatic. We thus conclude that the temperature fluctuation arises due to sound wave propagation. In Model H2, where the temperature of the infalling gas is comparable to virial temperature, shock does not occur and the temperature fluctuations are hardly seen, indicating that the formation of sound wave in other models is somehow related to shocks.

Inside the shock fronts temperature is nearly virial, high enough to emit X-ray. Entropy monotonically rises from the center to the shock front. That is, the gas near the center is heated up mainly through adiabatic compression , thus possessing relatively lower entropy there. Gas near the shock is, on the other hand, heated through shocks, which effectively transform kinetic energy of accreting gas into thermal energy at their surface. This explains relatively large entropy just inside the shock.

The feature that entropy is monotonically increasing outward is also seen in the SPH simulation by Evrard(1990) and in X-ray observations by Markevitch, Sarazin, & Irwin (1996). The wavy feature as seen in our results is, however, hardly seen in their results, although the simple comparison with their results is problematic because of their poor spatial resolution. Note that the regions with entropy decreasing outward are convectively unstable. Convective motions, if they occur, will smear out such a feature.

When observing real CGs with X-ray telescopes, we actually obtain an emission-weighted, line-of-sight projected temperature map. We thus need to check if the wavy patterns in the radial temperature profile can actually be observed without being washed out through integration along the line of sight. The example of such a map is shown for Model A in figure 7. In this figure we assumed the spatial resolution to be 0.1 Mpc, which corresponds to about 10 arc minutes for an object being located at $z = 0.01$, and the error of the temperature measurement to be 10%. Except for the inner two bins the temperature distribution is almost isothermal and coincident with the typical observational tendency. Still some fluctuations can be observed. In the central two bins the temperature is significantly higher than in others. In the observation of real CG, however, such high temperatures will not be observed due to the effect of radiative cooling and the existence of cD galaxies,
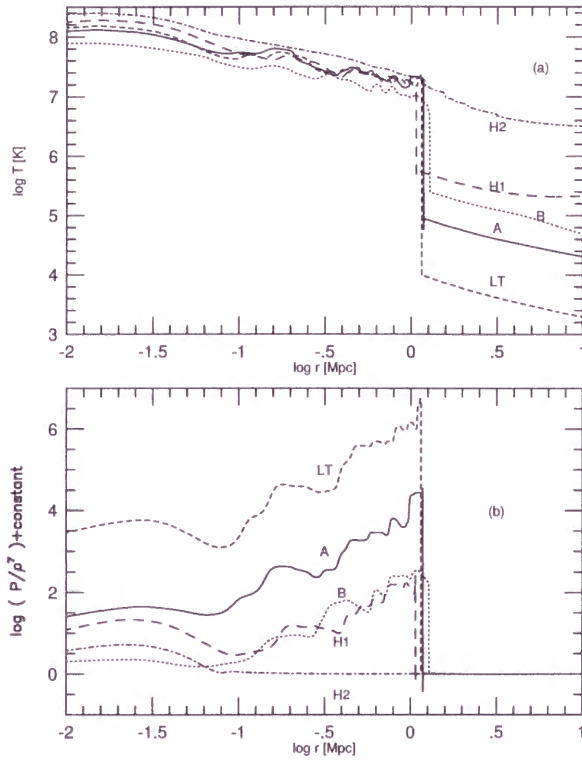
Figure 6: (a) Temperature profiles and (b) entropy profiles of each model at $z = 0$. Entropy is normalized to zero at the outer boundary. The different types of lines correspond to different models: Model A by the solid line; Model B by the dotted line; Model LT by the short dash line; Model H1 by the long dash line; and Model H2 by the dot-short dash line, respectively.
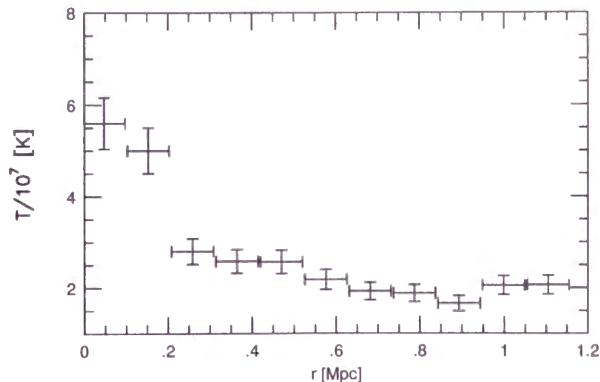
Figure 7: The emission-weighted, line-of-sight projected temperature map of Model A. We assumed the the spatial resolution to be 0.1 Mpc, which corresponds to about 10 arc minutes for an object being located at $z = 0.01$, and the the error of the temperature measurement to be 10%. Except for the inner two bins the temperature distribution is almost isothermal and coincident with the typical observational tendency.

which are not included in our calculations.

In our simulations thermal conduction is neglected. It is possible, however, that thermal conduction, if efficient, will erase temperature fluctuations on a small scale. It is thus worthwhile evaluating the conduction timescale in the simulated clusters. The conduction time scale is generally expressed as (cf. Sarazin 1988)

$$t_{\rm cond} \approx \frac{n_e l_{\rm T}^2 k_{\rm B}}{\kappa}, \tag{74}$$

where n_e is electron number density, $l_{\rm T}$ is the scale length of temperature gradient, $k_{\rm B}$ is the Boltzmann constant, and the thermal conductivity for hydrogen plasma is (Spitzer 1962)

$$\kappa \approx 4.6 \times 10^{13} \left(\frac{T_e}{10^8 {\rm K}}\right)^{5/2} \left(\frac{\ln \Lambda}{40}\right)^{-1} ({\rm erg s}^{-1} {\rm cm}^{-1} {\rm K}^{-1}), \tag{75}$$

where $\ln \Lambda$, Coulomb logarithm, is

$$\ln \Lambda = 37.8 + \ln \left[\left(\frac{T_e}{10^8 {\rm K}}\right)\left(\frac{n_e}{10^{-3} {\rm cm}^{-3}}\right)^{-1/2}\right]. \tag{76}$$

From equations (74) and (75), we derive

$$t_{\rm cond} \approx 3 \times 10^7 {\rm yr} \left(\frac{n_e}{10^{-3} {\rm cm}^{-3}}\right) \left(\frac{T_e}{10^8 {\rm K}}\right)^{-5/2} \left(\frac{l_{\rm T}}{0.1 {\rm Mpc}}\right)^2 \left(\frac{\ln \Lambda}{40}\right). \tag{77}$$

For Model A, for example, we find $t_{\rm cond} \sim 1.5 \times 10^8 {\rm yr}$ at $r \approx 0.1$ Mpc (where $n_e \sim 10^{-3} {\rm cm}^{-3}$, $T_e \sim 5 \times 10^7$ K, and $l_{\rm T} \sim 0.1$ Mpc) and $t_{\rm cond} \sim 1.5 \times 10^7 {\rm yr}$ at $r \approx 1 {\rm Mpc}$ (where

33

$n_e \sim 10^{-5} cm^{-3}$, $T_e \sim 2 \times 10^7$ K, and $l_T \sim 0.1$ Mpc). At both radii, hence, conduction seems to be efficient. The same is true for Model B. However, we should note that the usage of the classical conductivity (Spitzer 1962) is in question for CGs. In fact, we cannot explain the existence of cooling flows as long as we employ the classical one (Binney & Cowie 1981). Rather, it is suggested that tangled magnetic field (Rosner & Tucker 1989) or plasma instabilities (Pistinner & Shaviv 1996) are likely to suppress heat conduction significantly in CGs. Temperature fluctuations can then survive.

9.4 Sound Wave Propagation in ICM

To understand why the temperature, density, and entropy steadily increase with time even after the passage of the shock front and how sound waves arise and propagate outward, we check the balance between pressure gradient and gravity in the inner parts.

The gravitational force overcomes the pressure gradient force just inside the shock front. This causes radial gas inflow from outside. Therefore, gas is steadily adiabatically compressed by the infalling material from outside. Importantly, the ratio changes with time. Since the DM density profile hardly changes with time near the core, so does the gravity force; the ratio changes are purely due to the time and spatial variations of the pressure profiles of the gas. The force ratio is greater than unity near the center. This is because when ambient gas suddenly falls towards the center, pressure at the core will abruptly increase. This gives rise to an outwardly propagating sound wave. Note that the central point is a reflecting boundary in the case of spherical collapse (cf. subsection 2.2). We confirm that the radial infall systematically remains even after the passage of shock. In addition, we confirm fluctuation pattern propagating outwards with a speed roughly equal to the sound velocity, that is about 700 km s^{-1}.

Note that the property of the sound wave may depend on our assumption of spherical symmetry. It is open to question how such sound wave behaves in a realistic three-dimensional situation; i.e, when mass accretion takes place in a nonaxisymmetric way (e.g., by merger of multiple density condensations). However, it is at least plausible that at the initial collapse phase when a shock occurs a sound wave should be generated and start to propagate.

9.5 Evolution of The Shock Surface

As we have seen in subsection 9.4, the sound wave propagates outward, modulating the temperature profile. This also affects the shock front propagation, since sound speed inside the shock is three times greater than the front velocity in strong shock limits. We illustrate in figure 8 the radius of a shock surface (r_{shock}) as a function of the look-back time, the time measured from the present time backward; i.e., $t_{lb} = 0$ corresponds to the present time ($z = 0$). The different types of lines correspond to same models as in figure 6 except Model

34

Model	r_a (Mpc)	v_a (km s^{-1})
A	1.18	210
B	1.28	203
LT	1.15	207
H1	1.07	188
H2	—-	—-

Table 4: The arrival radius of shock surface at $z = 0$, r_a, and mean propagating velocity, v_a.
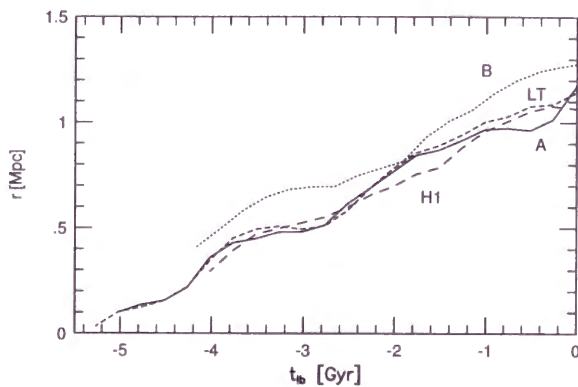

Figure 8: Time evolution of the radius of a shock surface, r_{shock}. The abscissa is the look-back time, time measured from the present time; $t_{\text{lb}} = 0$ at $z = 0$. Shock surface moves with a nearly constant velocity (~ 200 km s^{-1}). The different types of lines correspond to same models as in figure 6.

H2, where shock does not form. The Shock surface moves with nearly a constant velocity (~ 200km s^{-1}). The radius of shock surface at present, r_a, and the mean propagation velocity, v_a, are listed in table 4. Again, there are wavy features seen in this figure.

To understand the physics causing the modulating features, we plot the time variation of shock radius (r_{shock}, in the upper panel) and shock strength (in the lower panel) for Model A in figure 9. To evaluate the shock strength we use $T_7 \Delta S$ (in the lower panel) where T_7 is the pre-shock gas temperature in the unit of 10^7K and $\Delta S = S_{\text{in}} - S_{\text{out}}$ with S_{in} and S_{out} being specific entropies inside and outside the shock surface, respectively. Since this quantity is proportional to heat produced through shock heating, it is a good representation of the shock strength. Both panels show similar time modulations. This in turn creates the spatial modulation in the entropy profile, since the shock with modulating shock strength moves outward with time; namely, at the radius over which the shock passed
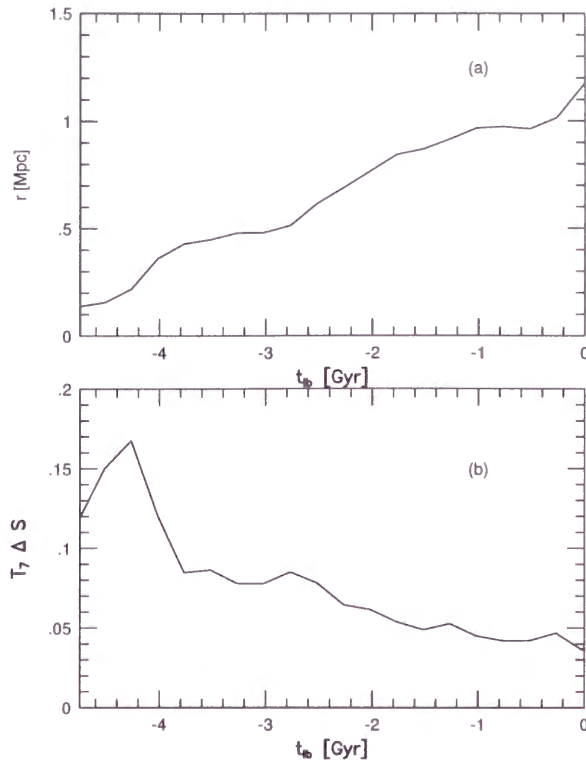
Figure 9: Evolution of the shock radius and shock strength of Model A. (a) Time evolution of r_{shock}. (b) That of $T_7 \Delta S$, where T_7 is the pre-shock gas temperature in the unit of 10^7K and ΔS is the jump in the entropy over the shock surface. This quantity is proportional to heat produced through shock heating.

with its maximum (minimum) strength, the radial entropy profile exhibits a rapid (or slow) rise outward. The time modulation in the shock strengths is likely to be caused by shock radius oscillation, and this oscillation is, as we discussed above, caused by the sound wave propagation. Note that while the wavy pattern in the temperature profile at a fixed radius varies with time because of sound wave propagation, the pattern in the entropy profile does not, since the entropy profile is unaffected by sound waves.

9.6 Evolution of X-Ray Luminosity

The time evolutions of the X-ray luminosity, $L(t_{\mathrm{lb}})$, and the normalized luminosity, $L_{\mathrm{n}}(t_{\mathrm{lb}}) \equiv L(t_{\mathrm{lb}})/L(t_{\mathrm{lb}} = 0)$, are plotted in figure 10 (a) and (b). When calculating luminosity, we assume thermal bremsstrahlung of optically thin plasma (Rybicki & Lightman 1979),

$$\varepsilon^{\mathrm{ff}} \equiv \frac{dW}{dV\,dt} = 1.4 \times 10^{-27} T^{1/2} n^2 \bar{g}_B \ (\mathrm{erg\ s^{-1} cm^{-3}}), \tag{78}$$

36

where T is gas temperature, n is number density, $\bar{g}_B$ is a frequency average of the velocity-averaged Gaunt factor. In this paper we set $\bar{g}_B = 1.2$. Emission from cool gas with temperature $T < 10^7$ K was neglected because we are interested in X-ray luminosity and only emission from the region where gas density is 10 times larger than the mean gas density is considered. Therefore, roughly the region where emissivity is 100 times larger is considered.

Figure 11 plots the evolution of L and L_n against z instead of t_{lb}.

In all the models except for Model H2, the luminosity rapidly rises just before the appearance of a shock wave, and then gradually rises afterwards. This behavior is due to the two distinct phases of the cluster evolution.

The first phase (before the formation of a shock wave): Through accretion of ambient gas towards the center gas in the central region is compressed adiabatically so that temperature and density there rapidly rise until the temperature reaches about virial. The rapid increase in L is thus due to a rapid rise in temperature of the central region.

The second phase (after the appearance of the shock wave): As the shock wave propagates outwards, high temperature region expands, thus increasing L. At the same time, gas inside the shock wave continues to be compressed adiabatically, thereby its emissivity being increased gradually.

In Model H2, the evolution is more rapid than the others. The distribution of gas density is less concentrated than others (see figure 12 in Model H2). Therefore, the ratio of emission from the central region to the total luminosity is relatively lower and luminosity evolves more rapidly with CG growing.

9.7 Dependence on the Cosmological Density Parameter

In this subsection, we compare the results of Model A ($\Omega_0 = 1$) and Model B ($\Omega_0 = 0.2$) to discuss the Ω_0 dependence of the cluster evolution under the condition that the perturbation amplitudes at $z = 10$ and the total masses contained in the perturbations are similar. The motivation here is not to discuss statistics of CGs distribution, but to examine how different expansion laws and average density of the Universe affect the evolution of the given perturbations.

From table 2, we see that the central DM density, $\rho_{DM,0}$, is proportional to Ω_0. The DM distribution is less concentrated in Model B than in Model A, because the ambient gas density is lower in a lower density universe so that a larger volume is needed to contain the same amount of mass ($\sim 10^{15} M_\odot$) initially. The absolute values of DM density are thus different among these models, but the shape of the DM density profiles are similar. This explains why nondimensional DM density profiles look similar among both models
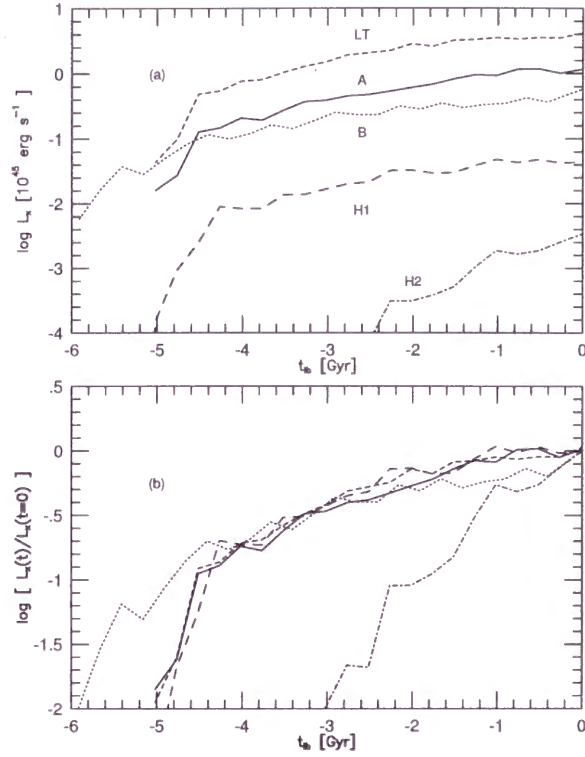
37

Figure 10: (a) Time evolution of X-ray luminosity, $L(t_{lb})$, and (b) that of normalized luminosity, $L_n(t_{lb}) \equiv L(t_{lb})/L(t_{lb} = 0)$. In all models except Model H2 L rapidly rises just before the generation of a shock wave, and then rises gradually afterwards. In Model H2 the evolution is more rapid than the others. The distribution of gas density is less concentrated than the others (see figure 12 in Model H2). Therefore, the ratio of emission from the central region to the total luminosity is relatively lower and luminosity evolves more rapidly with CG growing. The different types of lines correspond to same models as in figure 6.
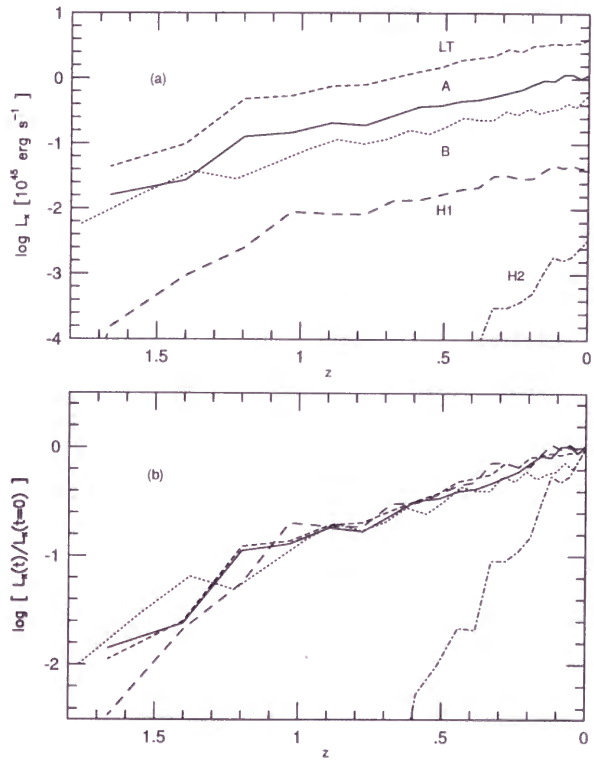
38

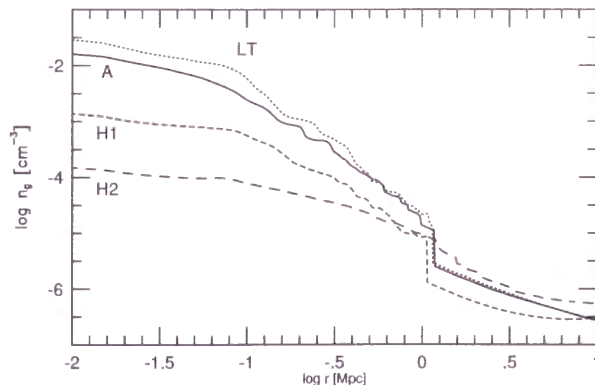Figure 11: Evolution of L and L_n plotted against z.

Figure 12: Gas density profiles at the present for Model A (solid line), Model LT (dotted line), Model H1 (short dash line) and Model H2 (long dash line).

(figure 4a). On the other hand, the central density of gas, $n_{gas,0}$, depends also on its initial entropy and is, hence, not strictly proportional to Ω_0 (see table 3). This is responsible for the differences in nondimensional gas density profiles among two models (figure 4b).

In both models X-ray luminosity rises, however, the increase in $L(t)$ is slower in Model B than in Model A. This tendency is more enhanced when $L(t)$ is plotted against t_{lb}, rather than against redshifts (see Fig. 10b, 11b). In the latter figure, the difference can be recognized at $z \sim 0.5$, but not at $z > 1$. This is because of a smaller amount of DM and gas surrounding a central condensation in a lower Ω_0 universe.

9.8   Dependence on the Initial Temperature of Gas

We calculated a four models with different initial temperatures (A, LT, H1, H2) to see how the initial temperature affects the later evolution. The temperature and entropy profiles at $z = 0$ of Models A, LT, H1, H2 are showed in figure 6. There is no significant difference among these models except for H2, especially in the structure inside the shock front. The thermal property of the gas outside the shock front has little influence on the thermal property of gas inside because of enormous entropy production at the shock surface. In Model H2 shock and entropy production dose not occur and small fluctuation of temperature and entropy profile cannot be seen.

On the other hand, the central densities are different among these models (figure 12). According to $n_{gas,0}$ estimated from the fitting data of table 3 and figure 12, the central density of Model LT is about three times greater than that of Model A. In the density profiles at $r > 0.3$ Mpc, however, any difference can hardly be seen.

In the central region, gas is adiabatically compressed until the temperature reaches about the virial temperature. So, a lower initial gas temperature results in a higher gas density, if the virial temperatures are the same in both models. However, the difference in the central

40

gas densities cannot be perfectly explained solely by this picture. If there is no entropy production (i.e., if gas is perfectly adiabatically compressed), the central density of Model LT should be about thirty times greater than that of Model A. This means, shock heating took away the information about the initial gas temperature also in the central region. Similar description is obtained in the relationship between Model A and H1.

Because of higher central gas density Model LT cluster is most luminous in X-ray than the others (figure 10a, 11b). Appreciable difference, however, cannot be seen in the evolutionary behavior of X-ray luminosity of these models except for Model H2 (figure 10b, 11b).

The evolutionary behavior of Model H2 is rather different from that of the others. Since initial gas temperature is high enough, the shock does not appear and gas evolves adiabatically without entropy production. The gas is not in free fall, but rather is partly supported by pressure as its temperature has nearly the virial value. Therefore the density profile of the gas is less concentrated than that of not only the DM but also the gas component of other models. Therefore, β_{gas} is rather smaller than the typical observational value (~ 0.8). Because of such loose gas distribution, the evolution of X-ray luminosity is quite rapid. The entropy profile, which is almost constant, is quite different from the results of Markevitch et al. (1996).

10   SUMMARY AND DISCUSSION

We carry out the numerical simulations of spherical clusters of galaxies with the shell model for DM and the second order up-wind TVD scheme for ICM to examine structural evolution of ICM. A shock front formed and moves outwards as gas accretes towards the cluster center, yielding a relatively flat temperature profile inside the shock front. The density and pressure profiles evolves in a self-similar fashion.

X-ray luminosity increases with time in two steps. At the initial collapse of DM gas in the central part is at first adiabatically compressed through accretion of ambient gas towards the center. Eventually, a shock wave appears near the center and X-ray luminosity rapidly rises until temperature increases and reaches about virial temperature via shock heating. In the late stage, in contrast, the luminosity rises only gradually, since the inner region already emits strong X-rays. The gradual brightening is due partly to the expansion of the inner high temperature region and partly to increasing X-ray emissivity of gas as the results of continuous adiabatic compression of the gas inside the shock.

If we compare two clusters with the same density fluctuation amplitudes at $z = 10$ and with the same total masses in different mean-density universes, the DM distribution is less concentrated in clusters in a lower density universe. Hence, X-ray luminosity of clusters rises more slowly than in a higher density universe.

The initial gas temperature has some influence on the gas density profiles. A higher initial temperature results in a lower central density and a less concentrated distribution

41

	$\rho_{DM}(r)$	$\rho_{gas}(r)$	$P(r)$	$r_{shock}(t)$
A	$r^{-2.6}$	$r^{-2.4}$	$r^{-3.0}$	$t^{0.90}$
Bertschinger(1985)	$r^{-2.25}$	$r^{-2.4}$	$r^{-2.9}$	$t^{0.89}$

Table 5: The comparison between the behavior of A1 and the self-similar solution of Bertschinger (1985)

(smaller β_{gas}). This corresponds to the case that reheating of the ICM e.g., by proto-galaxies is substantial. Thus, the inclusion of reheating process modifies the scaling law between X-ray luminosity and temperature in the way favored by the observed relation (NFW). Note that the epoch of the shock formation depends on the initial specific entropy at the core; in the presence of reheating process (so that the initial gas temperature is $\sim 10^7$K), specific entropy at the core is already high enough, and so the appearance of shock may be delayed. If the specific entropy is even higher so that the temperature of the infalling gas exceeds the virial value, the shock does not appear. In this case, sound wave propagation is hardly seen and luminosity evolution is more rapid. Importantly the gas density profile is less concentrated than the typical observed CGs, and the entropy profile is also quite different from the observational results by Markevitch et al. (1996). We thus reject such models.

In table 5 we compare the time dependent properties of Model A cluster and those of the self-similar solution by Bertschinger (1985). Both look very similar. Note that the self-similarity can be seen in all the calculated models. Although Einstein-de Sitter universe is assumed in Bertschinger (1985), we find that the self-similarity can also be found for cluster evolution in a low density universe ($\Omega_0 = 0.2, \lambda_0 = 0$).

Our results regarding the present profiles of density, temperature, and so on roughly coincide with those of the previous SPH simulations (Evrard 1990; NFW). However, the structure of the shock front, which was not well resolved in the previous SPH simulations, is now clearly captured in the present mesh-code simulations; our results show that hot gas of X-ray CG is separated with a definite boundary and that shock heating plays an important role for the heating process of ICM. We confirmed the persistence of radial infall of gas after the passage of the shock front. This results in adiabatic compression of the inner parts, inducing gradual temperature increase. We also found time variations in the strengths of the shock due to a sound wave propagation over the entire cluster, which modulates the radial distributions of temperature and density with relative amplitudes of about 10 %. If the temperature modulation will be observed with future X-ray mission (such as ASTRO-E), this can be used as a good probe to investigate the structure, especially, initial gas temperature and the mass distribution of CGs, since the sound wave properties sensitively depend on the shape and the depth of the gravitational potential well as well as initial

42

temperature.

Part III
A TWO-TEMPERATURE MODEL OF ICM

11   INTRODUCTION

Revealing temperature profiles of ICM is an important problem. In theoretical work concerning CG, isothermality of ICM is often assumed. In particular, the isothermal β model (Cavaliere & Fusco-Femiano 1976) is adopted in the conventional mass determination through X-ray observations, in the estimation of the Hubble constant (H_0) through Sunyaev-Zel'dovich (SZ) effect (Sunyaev & Zel'dovich 1972; Birkinshaw, Hughes, & Arnaud 1991), etc. However, deviation from a flat temperature profile becomes important at lower densities in the mass estimation using X-ray data (Evrard, Metzler, & Navarro 1996; Schindler 1996). Also in the H_0 estimation through SZ effect the non-isothermality is one important source of errors (Inagaki, Suginohara, & Suto 1995; Yoshikawa, Itoh, & Suto 1998). Therefore, accurate temperature profiles of ICM are required to improve such methods.

On the other hand, temperature maps of ICM provide us with useful information about CG. In merging clusters, characteristic temperature structures are expected to occur through shock heating and adiabatic compression. Some numerical simulations are especially focused on this problem (Schindler & Müller 1993; Ishizaka & Mineshige 1996; Roettiger, Loken, & Burns 1997; Ishizaka 1998; Roettiger, Stone, & Mushotzky 1998). In particular, off-center collisions are investigated by Ricker (1998). Comparing these results with the X-ray observational data , we can guess in what phase the merging clusters are (Fujita et al. 1996; Honda et al. 1996; Churazov et al. 1998; Donnelly et al. 1998; Davis & White 1998).

Recent X-ray observations with ASCA and ROSAT reveal the radial electron temperature distribution of ICM (Markevitch et al. 1996; Markevitch 1996; Markevitch, Sarazin, & Irwin 1996; Markevitch et al. 1997). In some clusters the observed electron temperature gradients correspond to the polytropic index, $\gamma(P \propto \rho^\gamma)$, of $\gamma = 1.5$ or even more (Markevitch 1996). On the other hand, $\gamma \simeq 1.2$ is expected for plasma mean temperature distribution derived by the self similar solution of Bertschinger (1985) and some numerical simulations (Evrard 1990; Katz & White 1993; Navarro, Frenk, & White 1995; Eke, Navarro & Frenk 1997; Takizawa & Mineshige 1998a; Bryan & Norman 1998). There is a discrepancy between the observed values and the theoretical expectations.

To explain the discrepancy between the observed electron temperature profiles and the theoretical suggestions on the mean temperature profiles consistently, we construct a model

of ICM incorporating properly the relaxation process between the ions and electrons. Fox & Loeb (1997) was the first to investigate the two-temperature nature of ICM. They construct the electron and ion temperature profiles by combining the self-similar solution by Bertschinger (1985) with the analytical evolutionary model of adiabatic two-temperature plasma which is originally found by Shafranov (1957). Chiéze, Alimi & Teyssier (1998) carried out the 3-D hydrodynamical simulations of two-temperature ICM. However, CGs only in the Einstein de Sitter universe were considered in the previous work concerning the two-temperature model of ICM. Since in a higher density universe CG form at more recent epoch (Richstone, Loeb, & Turner 1992), the previous work is restricted to the case in which a temperature difference is expected to be the largest among reasonable cosmological models. Therefore, it is necessary to study a two-temperature model of ICM in other cosmological models in order to confirm whether the temperature difference is really significant or not. This problem is also related to the dependence of temperature profiles on the cosmological parameters, which is discussed in some numerical simulations (Evrard et al. 1996; Eke et al. 1997). Furthermore, quantification of resultant temperature profiles by using polytropic indices is not fully discussed in the previous work, which is very important to compare the models with X-ray observations properly. Ettori & Fabian (1998) studied two-temperature ICM using simple analytic models and applied their results to the CG A2163. However they neglected the dynamical properties of ICM and assumed that all the ICM in CG is heated at the same time. This assumption is problematic to quantify the temperature profiles because the timescale of shock propagation in CG is comparable to the dynamical timescale and not much shorter than the age of the universe.

For these purpose, we apply the method of Fox & Loeb (1997) to the results of numerical simulations instead of the self-similar solution. Thus we can investigate two-temperature ICM quantitatively in cosmological models other than the Einstein de Sitter model. Studying the dependence of electron temperature profiles on cosmological models is another important purpose.

Part III of this thesis is organized as follows. In §12 we estimate the relevant timescales and spatial scales of ICM. In §13 we briefly review the adiabatic model of two-temperature plasma proposed by Fox & Loeb (1997). In §14 we described the method to calculate the ion and electron temperature profiles of ICM by combining a one-temperature ICM model with the adiabatic model by Fox & Loeb (1997). In §15 we describe the adopted numerical methods and initial conditions for simulations of CG. In §16 we present the results. In §17 we summarize the results and discuss their implications.

12 ORDER ESTIMATION

We consider fully ionized plasma which consists of electrons and ions. Only coulomb coupling is considered as the relaxation process. Then two-body relaxation timescale of a

x-particle, whose density is n_x and temperature is T_x, is (Spitzer 1962)

$$t_{xx} = \frac{m_x^{1/2}(3kT_x)^{3/2}}{5.71\pi n_x e^4 Z_x^4 \ln \Lambda},$$ (79)

where, m_x is the particle mass, Z_x is the particle charge number, e is the electron charge, k is the Boltzmann constant, and $\ln \Lambda$ is the Coulomb logarithm and approximated to be

$$\ln \Lambda \simeq 37.8 + \ln\left(\frac{T_x}{10^8 K}\right) - \frac{1}{2}\ln\left(\frac{n_x}{10^{-3}cm^{-3}}\right)$$ (80)

for $T_x > 4 \times 10^5$ K. Therefore, t_{ii} is larger than t_{ee} by a factor of the order of $(m_i/m_e)^{1/2}$.

On the other hand, the equilibrium timescale between ions and electrons is,

$$t_{ei} = \frac{3m_e m_i}{8(2\pi)^{1/2}n_i Z_i^2 e^4 \ln \Lambda}\left(\frac{kT_e}{m_e} + \frac{kT_i}{m_i}\right)^{3/2}.$$ (81)

Therefore, t_{ei} is grater than t_{ii} by a factor of $(m_i/m_e)^{1/2}$. In addition, this timescale can be comparable to or longer than the Hubble time in the outer region of CGs,

$$t_{ei} = 2.0 \times 10^8 yr\left(\frac{\ln \Lambda}{40}\right)^{-1}\left(\frac{n_i}{10^{-3}cm^{-3}}\right)^{-1}\left(\frac{T_e}{10^8 K}\right)^{3/2}.$$ (82)

Suppose that ICM is heated through the shock in accretion flow (Cavaliere, Menci, & Tozzi 1997). The shock primarily heats ions because the kinetic energy of a particle is proportional to the particle mass. In the post shock region the ions reach thermal equilibrium on a timescale of t_{ii} after they are heated through the shock. Within this time ion temperature is significantly higher than electron one. Eventually thermal energy is transported from the ions to the electrons through the Coulomb collisions between the ions and electrons and T_i becomes comparable to be T_e on timescale of t_{ei}. Note that $t_{ei} > t_{ee}, t_{ii}$.

Under such circumstance, the radial length, r_{tt}, over which the electron temperature is significantly lower than the ion temperature can be estimated as follows. Denote the propagation speed of the shock front by v_{shock}. Then, we have,

$$r_{tt} \simeq t_{ei} v_{shock}.$$ (83)

Using the strong shock approximation and neglecting the post-shock gas velocity compared with v_{shock}, we find

$$v_{shock} \simeq \frac{1}{3}v_{infall},$$ (84)

where v_{infall} is the infalling velocity of the gas, which is related to the post-shock gas temperature, T. The kinetic energy of infalling gas is nearly equal to the thermal energy of the post shock gas; namely

$$\frac{1}{2}m_p v_{infall}^2 \simeq k_B T.$$ (85)

Therefore, using the equations (82), (83), (84), and (85), we derive

$$r_{\mathrm{tt}} \simeq 1.1 \times 10^{-1} \mathrm{Mpc} \left(\frac{\ln \Lambda}{40} \right)^{-1} \left(\frac{n_{\mathrm{i}}}{10^{-3} \mathrm{cm}^{-3}} \right)^{-1} \left(\frac{T_{\mathrm{e}}}{10^{8} \mathrm{K}} \right)^{-2}. \tag{86}$$

Importantly this is smaller by about one order of magnitude than the spatial scale of CGs. Note that the higher temperature is, the wider becomes the region where the temperature difference between ions and electrons is significant.

Another important timescale related to ICM is the radiative cooling timescale, t_{c}. Since thermal bremsstrahlung is the dominant cooling process in ICM, we have

$$t_{\mathrm{c}} = 8.5 \times 10^{10} \mathrm{yr} \left(\frac{n_{\mathrm{e}}}{10^{-3} \mathrm{cm}^{-3}} \right)^{-1} \left(\frac{T_{\mathrm{e}}}{10^{8} \mathrm{K}} \right)^{1/2}. \tag{87}$$

From equations (82) and (87) we find,

$$\frac{t_{\mathrm{ei}}}{t_{\mathrm{c}}} = 2.3 \times 10^{-3} \left(\frac{\ln \Lambda}{40} \right)^{-1} \left(\frac{T_{\mathrm{e}}}{10^{8} \mathrm{K}} \right). \tag{88}$$

Hence t_{c} is always longer than t_{ei} in the typical ICM, and thus we can safely neglect cooling effects as far as we are concerned with the overall cluster structure.

On the other hand, the age of CG, t_{age}, is of the order of 10^{9} or 10^{10} yr. Therefore, as long as heating from galaxies can be neglected, we can divide intra-cluster space into three regions according to the magnitudes of these three timescales, t_{ei}, t_{c}, and t_{age} as follows:

1. The central higher density region where $t_{\mathrm{ei}} < t_{\mathrm{c}} < t_{\mathrm{age}}$. Radiative cooling is important but ICM can be regarded as one-temperature fluid. This situation corresponds to the so-cold 'cooling flow'.

2. The middle region where $t_{\mathrm{ei}} < t_{\mathrm{age}} < t_{\mathrm{c}}$. We can regard ICM as adiabatic one-temperature fluid.

3. The outer lower density region where $t_{\mathrm{age}} < t_{\mathrm{ei}} < t_{\mathrm{c}}$. Radiative cooling can be negligible and the electron temperature is considerably lower than the ion temperature.

13 EVOLUTION OF ADIABATIC TWO-TEMPERATURE PLASMA

The formulation here is based on Fox & Loeb(1997). We neglect thermal conduction, which is the case if tangled magnetic fields suppress conduction. The Laglangean time evolution

of the electron temperature, T_e, and the mean temperature, $\bar{T} = (n_e T_e + n_i T_i)/(n_e + n_i)$, in the adiabatic fluid element is,

$$\frac{dT_e}{dt} = \frac{T_i - T_e}{t_{ei}} + (\gamma - 1)\frac{T_e}{n}\frac{dn}{dt}, \tag{89}$$

$$\frac{d\bar{T}}{dt} = (\gamma - 1)\frac{\bar{T}}{n}\frac{dn}{dt}, \tag{90}$$

where T_i is the ion temperature, n is the gas density, and $\gamma = 5/3$, is the ratio of specific heat. Introducing the temperatures normalized by $\bar{T}$, $\tilde{T}_e \equiv (T_e/\bar{T})$ and $\tilde{T}_i \equiv (T_i/\bar{T})$, we find,

$$\frac{d\tilde{T}_e}{dt} = \frac{\tilde{T}_i - \tilde{T}_e}{t_{ei}}. \tag{91}$$

Note that t_{ei} is proportional to $\tilde{T}_e^{3/2} \ln \Lambda$, since in the post-shock region the gas behaves adiabatically ($\bar{T} \propto n^{2/3}$). Thus $t_{2s} \equiv t_{ei}(t)\tilde{T}_e(t)^{-3/2}$ is constant in time, if we neglect the small change due to the Coulomb logarithm. Now equation (91) becomes

$$\frac{d\tilde{T}_e}{dt} = \frac{1}{t_{2s}}\left(\frac{n_i + n_e}{n_i}\right)(1 - \tilde{T}_e)\tilde{T}_e^{-3/2}. \tag{92}$$

Since ICM is almost perfectly ionized, the ratio of $(n_i + n_e)/n_i$ can be regarded as constant. Thus equation (92) can be integrated analytically. If we assume the pre-shock $\tilde{T}_e$ equal to zero, the solution for the fluid element which has passed the shock front at $t = t_s$ is,

$$t - t_s = t_{2s}\left(\frac{n_i}{n_i + n_e}\right)\left[\ln\left(\frac{1 + \sqrt{\tilde{T}_e}}{1 - \sqrt{\tilde{T}_e}}\right) - 2\sqrt{\tilde{T}_e}\left(1 + \frac{\tilde{T}_e}{3}\right)\right]. \tag{93}$$

Thus we can obtain the Laglangean time evolution of $\tilde{T}_e$ of the fluid element after the passage through the shock by solving equation (93).

14   NUMERICAL METHOD

Using equation (93) we can construct the temperature profiles at $t = t_0$, $T_e(r, t_0)$ and $T_i(r, t_0)$, as follows. First, we give the velocity field of the gas, $v(r, t)$, the shock radius, $r_{shock}(t)$, and the equilibrium timescale of the fluid element at the passage through the shock front, $t_{2s}[r_{shock}(t)]$, using some analytical models or numerical simulations presented later. Then we can calculate the Laglangean path of the fluid element which passed the shock surface at $t = t_s$, $R(t; t_s)$, by solving the ordinary differential equation,

$$\frac{dR}{dt} = v(R(t; t_s), t), \tag{94}$$

48

with the appropriate initial condition,

$$R(t_\mathrm{s}; t_\mathrm{s}) = r_\mathrm{shock}(t_\mathrm{s}). \tag{95}$$

Integrating differential equation (94) for various t_s, we obtain $r_0 = R(t_0; t_\mathrm{s})$, the radius which the fluid element that passed the shock at $t = t_\mathrm{s}$ resides at $t = t_0$, as a function of t_s. Thus we can regard $t_0 - t_\mathrm{s}$ as a function of the radius,

$$t_0 - t_\mathrm{s} = f(r; t_0). \tag{96}$$

Using the equations (93) and (96), and the model of $t_{2\mathrm{s}}[r_\mathrm{shock}(t_\mathrm{s})]$, we can solve $\tilde{T}_\mathrm{e}$ at $t = t_0$ as a function of r. Finally, we obtain $T_\mathrm{e}(r)$ and $T_\mathrm{i}(r)$ using $\tilde{T}_\mathrm{e}(r)$ and the model of $\bar{T}(r)$.

15   THE SIMULATIONS

15.1   Numerical Method

To give $v(r,t)$, $r_\mathrm{shock}(t)$, etc, we have performed numerical simulations of a spherically symmetric CG. For dark matter (DM), we use the shell model (Hénon 1964). We set the number of shells, N, equal to 5000. As for gas on the other hand, we use 1-dimensional, spherically symmetric, total variation diminishing (TVD) code with minmod limiter (Hirsch 1990). Note that TVD code is one of the most powerful tools to treat shocks. One mesh spacing corresponds to $\Delta r = 0.005/(1 + z)$ Mpc. We assume that the gas is ideal, with $\gamma = 5/3$. As to the boundary conditions, the inner edge is assumed to be a perfectly reflecting point. The outer edge is assumed to be a perfectly transmitting surface. The basic equations and the numerical method used here are fully described in §2 of Takizawa & Mineshige (1998a).

15.2   Models and Initial Conditions

In this paper, all of the calculations are carried out from $z_\mathrm{ini} = 10$ to the present time ($z_0 = 0$). The cosmological models which we adopt are $(\Omega_0, \Lambda_0) = (1.0, 0.0)$ (ED), $(\Omega_0, \Lambda_0) = (0.2, 0.0)$ (OP), and $(\Omega_0, \Lambda_0) = (0.2, 0.8)$ (FL). The Hubble constant, H_0 is set to be $H_0 = 100 \mathrm{kms}^{-1}\mathrm{Mpc}^{-1}$ in the transformations of length and time coordinates. We set $\Omega_\mathrm{b} = 0.012h^{-2}$ in all models taken from the nucleosynthesis determination (Walker et al. 1991). Note that $\Omega_\mathrm{DM} = \Omega_0 - \Omega_\mathrm{b}$.

We make initial density profiles in the same manner as Peebles (1982). At first we prepare N concentric shells with a constant density equal to Ω_DM at $z_\mathrm{ini} = 10$. Then, a density fluctuation is introduced by perturbing the radius and velocity of each shell following

$$r_i = r_i^{(0)}\left\{1 - \frac{1}{3}\bar{\delta}[r_i^{(0)}]\right\}, \tag{97}$$

49

$$u_i = H(z_{\text{ini}})r_i^{(0)}\left\{1 - \frac{1}{3}(1 + \Omega^{0.6})\bar{\delta}[r_i^{(0)}]\right\}, \tag{98}$$

where $r_i^{(0)}$ is the unperturbed coordinate, $\bar{\delta}(r)$ represents the mean density fluctuation inside r, which is derived from the density fluctuation field (specified below) within r, and $H(z_{\text{ini}})$ is the Hubble constant at $z = z_{\text{ini}}$. Here, we used the Zel'dovich approximation (Zel'dovich 1970) and the approximation of $d\log D_1/d\log a \simeq \Omega^{0.6}$, where D_1 is the linear perturbation growth rate for the growing mode and a is the scale factor (see Suto 1993).

The initial conditions of the density fluctuation field, $\delta(r)$, are generated by applying the Hoffman-Ribak method (Hoffman & Ribak 1991; van de Weygaert & Bertschinger 1996) to spherical systems (see §A.1). We constrained in such a way that there exist initially density enhancements on 1 Mpc scale whose amplitudes correspond to 3σ level in the CDM power spectrum. The normalization is $\sigma_8 = 1$ in each cosmological model, which was obtained from the observation of the nearby galaxy distribution (see Suto 1993).

The initial conditions of gas are set as follows. At first, gas density was everywhere taken to be the mean baryon density of the universe at $z = 10$, and the temperature of the gas $(T_{\text{gas,i}})$ was constant everywhere; $T_{\text{gas,i}} = 10^7$K in all models. We then add the adiabatic fluctuation in such a way that the ratio of the DM density and the gas density remains the same. Note that after the perturbation is added, the gas temperature distribution becomes nonuniform, accordingly. Moreover, note that temperature of the infalling gas at $z \sim 1$ is sufficiently lower than virial temperature, since the gas expands adiabatically following the cosmological expansion.

16 RESULTS

The overall evolution of the simulated CG is essentially the same as that presented by Takizawa & Mineshige (1998a). Thus we concentrate on showing the results of the temperature profiles, mass estimation, and so on.

16.1 Temperature Profiles

Figure 13 shows radial distribution the $T_{\text{e}}(r)$ (solid line), $T_{\text{i}}(r)$ (dotted line), and $\bar{T}(r)$ (short dashed line) of Model ED at $z = 0$. At $r < 0.6$Mpc T_{e} is very close to T_{i}, while, at $r > 0.6$Mpc the electron temperature is considerably lower than the ion temperature and the discrepancy gets increased outward. At $r \simeq 1$Mpc, the electron temperature is only a half of the mean temperature. Small scale fluctuations in the temperature profiles are due to the sound wave propagation in ICM (Takizawa & Mineshige 1988a).

In real X-ray observations what is actually obtained is an emissivity-weighted, line-of-sight projected electron temperature map, which is displayed in Figure (14) for model ED. In this figure, we assumed the spatial resolution to be 0.25 Mpc, which corresponds to
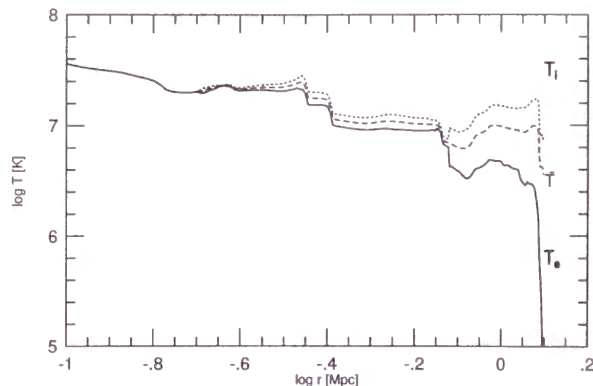
Figure 13: The profiles of the T_e (solid line), T_i (dotted line), and $\bar{T}$ (short dashed line) of Model ED at $z = 0$. At $r < 0.6$ Mpc $T_e \sim T_i$, whereas at $r > 0.6$ Mpc T_e is considerably lower than T_i and the discrepancy gets enhanced outward. At $r \simeq 1$ Mpc, $T_e \sim \bar{T}/2$. Small scale fluctuations in the temperature profiles are due to the sound wave propagation in ICM.

about 6' for an object located at $z = 0.05$, and the error of the temperature measurement to be 20 %. Also in this map we can clearly see that the electron temperature decreases outward.

To estimate the temperature gradients both for T_e and $\bar{T}$, we measure the polytropic indexes, γ_p, in the usual way. We fit the density profile by the β-model and the temperature profile by the polytropic model as follows,

$$n(r) = n_0 \left[1 + \left(\frac{r}{r_c} \right)^2 \right]^{-3\beta/2}, \tag{99}$$

$$T(r) \propto n(r)^{\gamma_p - 1} \tag{100}$$

where n_0, r_c, and β is the fitting parameters of the β-model. We fit the resultant density profile only inside the shock front. The data are fitted by chi-square fitting. We assume that the variance in any quantity is proportional to its square ($\delta f/f = $ const.) because our main purpose is not to simulate observations with a specific instrument but to obtain the intrinsic profiles of our calculated results. The results of the fitting are summarized in Table 6 and the corresponding polytropic indices are listed in Table 7. From Table 6 we find that the β values are somewhat bigger than those typically observed. On the other hand, our results are well coincident with the self-similar solution by Bertschinger (1985). Thus the bigger β values are probably due to the assumption of spherical symmetry and neglect of angular momentum of gas. If the initial gas temperature is higher, which corresponds to the case that reheating of the ICM, e.g., by protogalaxies, is substantial, β values can be smaller (Metzler & Evrard 1994; Takizawa & Mineshige 1988a). From Table 7 we find
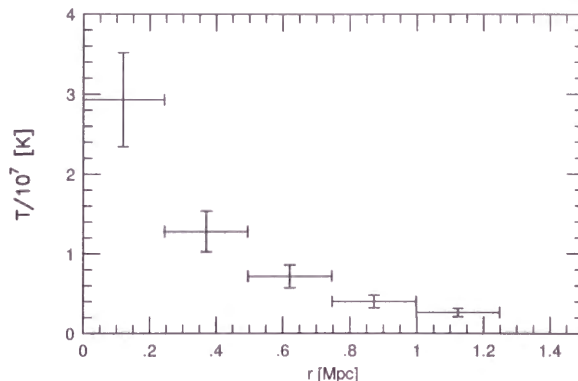
51

Figure 14: Emissivity weighted, line-of-sight projected electron temperature profile of Model ED at $z = 0$. Here we assumed the spatial resolution to be 0.25 Mpc, which corresponds to about 6' for an object located at $z = 0.05$, and the error of the temperature measurement to be 20 %. Clearly the electron temperature decreases outward.

Model	n_0 $(10^{-3}\mathrm{cm}^{-3})$	r_c (Mpc)	β
ED	1.16	0.067	0.793
OP	3.64	0.104	0.815
FL	1.45	0.155	0.903

Table 6: Density profiles of gas at $z = 0$.

that the polytropic indices of the electron temperature profiles are $\gamma_p \sim 1.5$, which are systematically larger than those of the mean temperature profiles, $\gamma_p \sim 1.3$.

The specific entropy profiles derived from the electron temperature $[S_e \propto \ln(T_e/\rho^{\gamma-1})]$, and from the mean temperature $[\bar{S} \propto \ln(\bar{T}/\rho^{\gamma-1})]$, are shown in Figure 15 by the solid and dotted lines, respectively. Entropy is normalized to be zero at the inner boundary. The latter $\bar{S}$ rises outward, which is characteristic of the ICM heated through the shock (Evrard 1990; Takizawa & Mineshige 1998a). The former S_e, in contrast, rises outward as the case only in the inner region ($r < 0.6$Mpc), stays nearly constant in the middle region, and falls outward in the outer region.

16.2   Dependence of Fitting Parameters on Size of Fitting

We fit the calculated density profile inside the shock front by equation (99) and listed the fitting results in Tables 6 and 7. However, it is possible that the fitting results can be influenced by the position of the outer edge of the region used for the fitting. In real X-ray

52

Model	γ_{p} of T_{e}	γ_{p} of $\bar{T}$
ED	1.55	1.35
OP	1.44	1.34
FL	1.51	1.37

Table 7: Polytropic indices of T_{e} and $\bar{T}$ at $z = 0$.
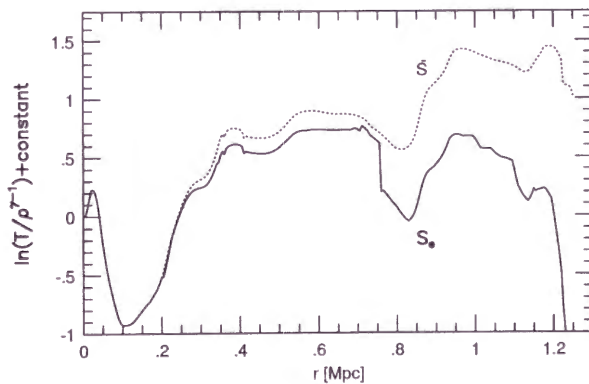
Figure 15: The specific entropy profiles derived from the electron temperature $[S_{\mathrm{e}} \propto \ln(T_{\mathrm{e}}/\rho^{\gamma-1})]$, by the solid line and from the mean temperature $[\bar{S} \propto \ln(\bar{T}/\rho^{\gamma-1})]$, by the dotted line, respectively. Entropy is normalized to be zero at the inner boundary.
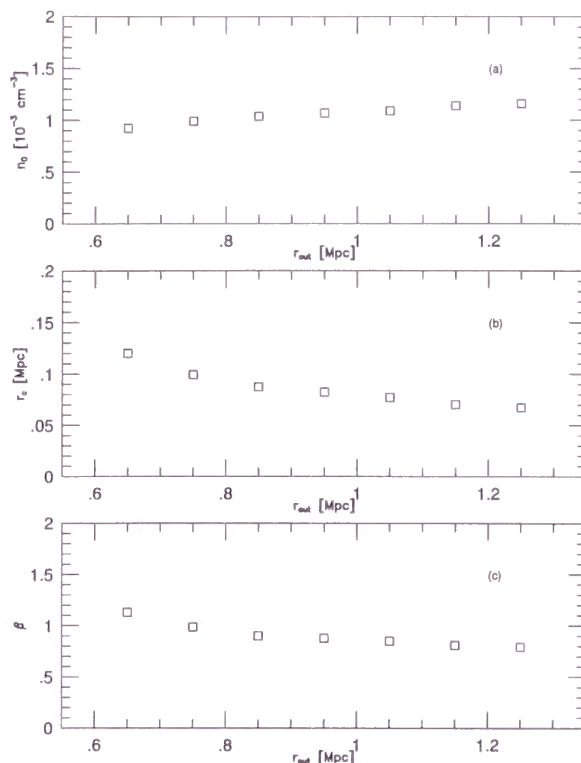
Figure 16: The dependence of the parameters related to the density profile (n_0, r_c, and β) on $r_{\rm out}$, the radius of the outer edge of the region used for fitting. It is found that these parameters are insensitive to the outer edge radius as long as $r_{\rm out} > 0.8$.

observations the outer edge of the X-ray emitting region is perhaps inside the shock front. To assess this effect we fit the density and temperature profiles inside various radii for Model ED and list the dependence of the fitting results related to the density profile (n_0, r_c, and β) on the outer-edge radius ($r_{\rm out}$) in Figure 16. It is found that these parameters are insensitive to the outer radius as long as $r_{\rm out} > 0.8$ Mpc. In density profiles, therefore, we can safely neglect the influence of the outer edge. This fact is actually expected because of the self-similar nature of the gas density profile (Bertschinger 1985; Takizawa & Mineshige 1998a).

On the other hand, the dependence of $\gamma_{\rm p}$ on $r_{\rm out}$ is rather different. Figure 17 shows that $\gamma_{\rm p}$ derived from $T_{\rm e}$ (by closed squares) monotonically increase outward whereas $\gamma_{\rm p}$ derived from $\bar{T}$ (by open square) does not exhibit systematic changes. When we calculate a polytropic index from X-ray observational data, thus, the resultant value could be subjected to large errors arising from the finite detection limit, background noise, and so on.

The results of model OP and FL are essentially the same as those of model ED. Although there is a simple self-similar solution only for model ED, self-similar nature is also expected
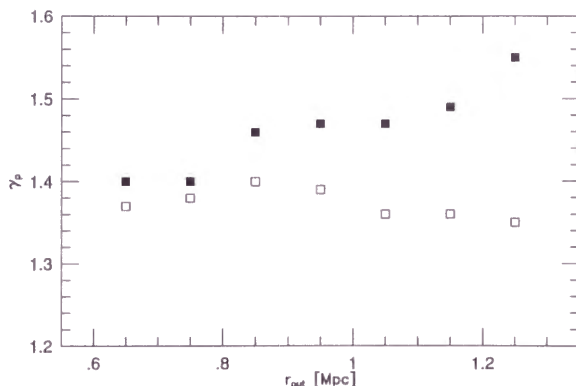
Figure 17: The dependence of γ_p on r_{out}. We find that γ_p obtained from T_e (closed squares) increases as r_{out} increases, whereas γ_p obtained from $\bar{T}$ (open squares) is insensitive to r_{out}.

both in OP and FL (Takizawa & Mineshige 1988a).

16.3 Mass Estimation

Since the observed electron temperature significantly deviates from the mean temperature that determines the dynamics of the system, the total mass of CG is probably underestimated if hydrostatic equilibrium is calculated based on the electron temperature map. When ICM is assumed to be isothermal we usually use the emissivity-weighted mean temperature, which is more like the temperature in the central high-density region. Thus, the underestimation of the mass is practically negligible. When the electron temperature profile is used, conversely, the mass can be seriously underestimated. Hence the mass derived from the assumption of hydrostatic equilibrium, $M_{hydro}(r)$, is,

$$M_{hydro}(r) = \frac{3kT_0\beta\gamma_p}{\mu m_p G} r \frac{(r/r_c)^2}{[1 + (r/r_c)^2]^{1+3\beta(\gamma_p-1)/2}}. \tag{101}$$

Figure 18 depicts the ratio of M_{hydro} to the actual mass as a function of radius. The solid line represents the ratio calculated based on $T_e(r)$ and the dotted line represents that based on $\bar{T}(r)$. The mass derived from T_e is underestimated by almost 50 % because of the lower electron temperature. Note that the mass derived from $\bar{T}$ is also underestimated by about 10 % due to the bulk motion of the gas (Takizawa & Mineshige 1998b).

In the central region M_{hydro} based on T_e and $\bar{T}$ are both larger than the actual mass. This is due to the fitting errors of temperature profiles. Since the core radii are different between the density and temperature profiles, polytropic model cannot describe the our results well in this region.
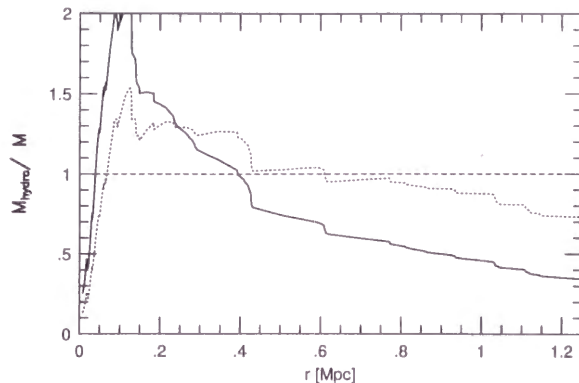
55

Figure 18: The ratio of M_{hydro} to the actual mass. The solid line is the result based on $T_e(r)$ and the dotted line is that based on $\bar{T}(r)$. The mass derived from T_e is underestimated by almost 50 % because of the lower electron temperature. Note that the mass derived from $\bar{T}$ is also underestimated by about 10 % due to the bulk motion of the gas

17 SUMMARY AND DISCUSSION

We constructed the models of ICM, incorporating the relaxation process between the ions and electrons. From the simple order estimation, we find that the electron temperature is well below the ion temperature in the outer region of CG and that such a lower T_e region spreads over a Mpc scale in typical CG. In addition, the hotter CG is, the wider becomes the two-temperature region. Comparing three relevant timescales in ICM (the age of CG, radiative cooling, and equilibrium timescales between ions and electrons), we can divide ICM into three regions; from the center outward, the cooling dominant, one-temperature region, adiabatic, one-temperature region, and adiabatic, two-temperature region.

We calculate the temperature profiles of two-temperature ICM combining the spherically symmetric, N-body and hydrodynamic simulations for three different cosmological models with the adiabatic two-temperature plasma model by Fox & Loeb (1997). While the polytropic indices of the mean temperature profiles are $\simeq 1.3$, those of the electron temperature profiles are $\simeq 1.5$. As a consequence, the specific entropy profiles derived from the electron temperature are rather flat.

We examine the dependence of the fitting parameters on the radius of the outer edge of the region used for the fitting when the density profile is fitted by the β-model and the temperature profile by the polytropic model. The fitting results of the density profile and mean temperature profile is insensitive to the outer edge. On the other hand, the polytropic index derived from the electron temperature rises as the outer-edge radius increases.

The total mass of CG is underestimated about 50 % when we use the electron temperature profile though the underestimation is negligible when we assume that ICM is isothermal and adopt emission-weighted mean temperature as the temperature of ICM.

56

We confirm that temperature difference between ions and electrons in ICM is substantial in cosmological models other than the Einstein de Sitter model. The polytropic indices of electron temperature profiles are insensitive to the cosmological models in the range of our calculations. Note that the baryon density of these models is set to be the same. If the baryon fraction is set to be constant in each model, the result will probably changes because the equilibrium timescale is sensitive to the baryon density.

In general our resultant electron-temperature profiles tend to have steeper gradients than those of Ettori & Fabian (1998). They assumed that all the ICM in CG is heated at the same time and that ICM is in hydrostatic equilibrium. On the other hand, in our calculations the ICM in the outer region is heated more recently than that in the inner region because the shocks propagate at finite speed. Furthermore, gradual radial infall persists inside the shock fronts and makes the two-temperature region slightly compress inward. (Takizawa & Mineshige 1998a). Thus the two-temperature region of our results becomes wider than those of Ettori & Fabian (1988).

Although only spherical accretion is considered in this paper, there may also arise asymmetric merging of comparable clumps in reality. It is possible that shocks occurring in merging events will also generate the temperature difference between ions and electrons. In this case it is believed that a bow shock with an arc shape is formed just between the centers of two substructures (Schindler & Müller 1993; Ishizaka & Mineshige 1996; Roettiger et al. 1997; Ishizaka 1998). In the post-shock region the energy is transported from ions to electrons but that timescale changes along the shock front since the timescale is sensitive to the density of ICM. Therefore, if we consider the temperature difference between ions and electrons, the location of the observed hot gas region is probably shifted and the shape is more deformed in comparison with the results of the former simulations (Takizawa 1999; see §A.2).

We consider only the classical coulomb coupling as the relaxation process between ions and electrons. It is possible, however, in ICM more efficient relaxation processes may be effective (McKee & Cowie 1977; Pistinner, Levinson, & Eichler 1996). In this case the equilibrium timescale can be shorter than the value given by equation (82). Therefore, the temperature difference between ions and electrons can be less and polytropic indices can be smaller than our results. If magnetic field exits in ICM, it is possible that electrons are also significantly heated in shocks by MHD instabilities. Also in this case the temperature difference between ions and electrons can be less.

We neglect the heating process from the galaxies to ICM. If thermalized hot gas is injected to ICM from the galaxies, temperature difference could be less. Furthermore, in this case the preheating of the ICM influences the density profile and mean temperature profile (Metzler & Evrard 1994; Navarro et al. 1995; Takizawa & Mineshige 1998a). Since heavy elements like iron are detected in ICM at redshift up to $z \simeq 1$ (Hattori et al. 1997), this effect should be considered to construct a more realistic model. In such a study the adiabatic model like Fox & Loeb (1997) cannot be adopted. Thus non-adiabatic models or

fully two-fluid simulations like Chiéze et al. (1998) are required.

A.1 THE HOFFMAN-RIBAK METHOD FOR SPHER-ICAL SYSTEMS

We consider a random homogeneous and isotropic Gaussian field f with zero mean which is defined by its power spectrum $P(k)$. When f is subjected to linear constraints, $g = Cf$, then the constrained Gaussian field f is realized as follows (Hoffman & Ribak 1991),

$$f = \tilde{f} + MC^\dagger Q^{-1}(g - C\tilde{f}),\tag{A.1.1}$$

where $\tilde{f}$ is an unconstrained random Gaussian field whose power spectrum is $P(k)$, M is the two-point correlation matrix obtained from $P(k)$, and $Q = CMC^\dagger$.

In general three dimensional case, $\tilde{f}$ is described by its Fourier components $\tilde{f}_{\mathbf{k}}$,

$$\tilde{f}(\mathbf{r}) = \frac{1}{(2\pi)^3} \int \tilde{f}_{\mathbf{k}} \exp(i\mathbf{k}\mathbf{r}) d\mathbf{k}.\tag{A.1.2}$$

However, to generating the initial conditions which can be used for our spherical symmetric simulations, we should construct $\tilde{f}$ as a function of only r instead of $\mathbf{r}$. Since $\tilde{f}$ is isotropic $\tilde{f}(r)$ is obtained as follows. In spherical systems it is convenient to expand $\tilde{f}(\mathbf{r})$ in spherical harmonics times spherical Bessel functions j_l (Binney & Quinn 1991). A plain wave is expanded in these functions as follows,

$$\exp(i\mathbf{k}\mathbf{r}) = 4\pi \sum_{l=0}^{+\infty} \sum_{m=-l}^{+l} i^l j_l(kr) Y_l^{m*}(\theta_k, \phi_k) Y_l^m(\theta_r, \phi_r).\tag{A.1.3}$$

Integrating this for the tangential components we find,

$$\int \exp(i\mathbf{k}\mathbf{r}) d\mathbf{k} = 4\pi \int j_0(kr) k^2 dk.\tag{A.1.4}$$

We can assume that $\tilde{f}_{\mathbf{k}} = \tilde{f}_k$ because of isotropy of $\tilde{f}$. Thus we obtain,

$$\tilde{f}(r) = \frac{1}{2\pi^2} \int \tilde{f}_k \frac{\sin kr}{kr} k^2 dk.\tag{A.1.5}$$

A.2 TWO-TEMPERATURE ICM IN MERGING CLUSTERS OF GALAXIES

It is expected that rather complex ICM temperature structures occur in cluster mergers through shock heating and adiabatic expansion and compression. However, timescale surviving complex temperature structure is an order of 10^9 yr, which is comparable to t_{ei} of equation (81). Thus, two-temperature nature of ICM should be considered properly in cluster mergers. Recently, Takizawa (1999) investigates the evolution of ICM during a cluster merger, explicitly considering the relaxation process between the ions and electrons by N-body and hydrodynamical simulations. We briefly introduce their results in this appendix.

Figure 19 shows the results of a head-on collision between equal-mass $(0.5 \times 10^{15} M_\odot)$ clusters. In the contracting phase (upper and middle panels) two-temperature nature is not important since the shock is nearly a standing shock and the equilibrium timescale of heated gas originally located in the center of subclusters is shorter than $\sim 10^8$ yr. On the other hand, in the expanding phase (lower panels), electron and mean temperature distribution is quite different. The hottest component (~ 20 keV) cannot be seen in the electron temperature map because thermal energy of ions generated by the shock has not be transported to electrons yet. In addition, it is found that temperature difference between ions and electrons becomes larger in the directions tilted by the angles of $\pm 45°$ with respect to the collision axis. The reason is that the gas with shorter equilibrium timescale originally located in the central part moves both in the parallel and perpendicular directions to the collision axis since gas outflow occurs in these directions.

The results is similar in the case of an absorption of a smaller cluster by a larger one (Figure 20), where mass ratio of larger and smaller one is 4 : 1.
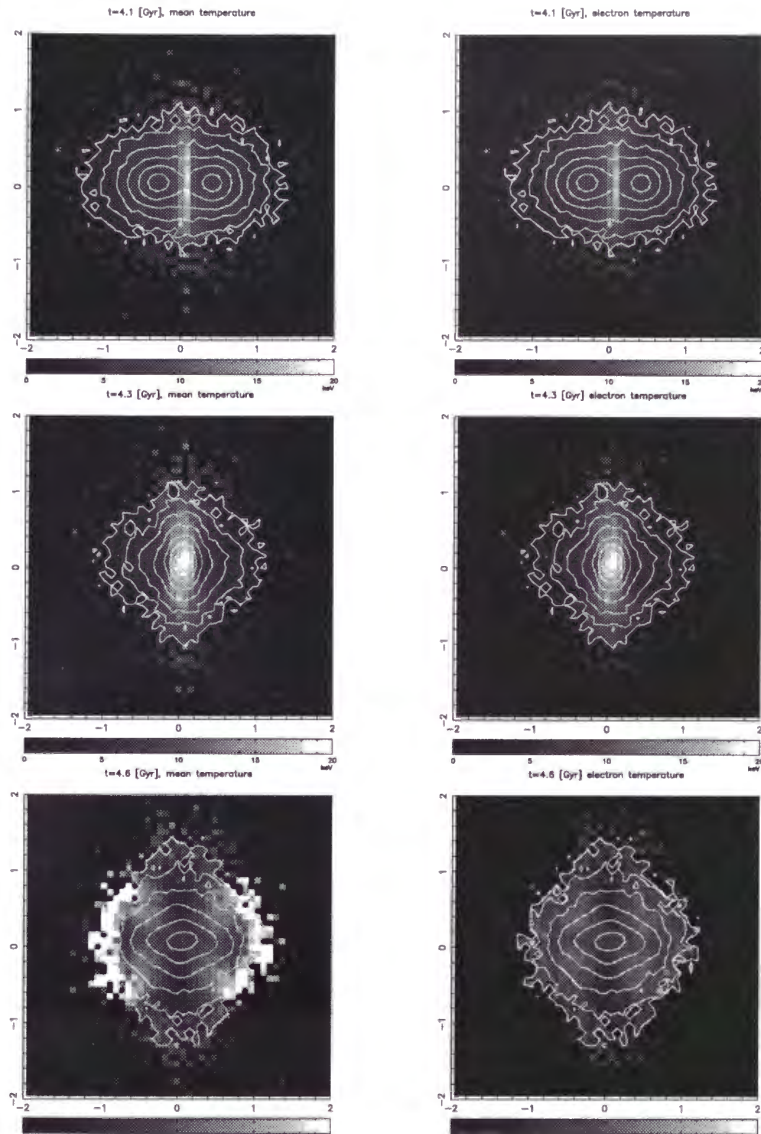
Figure 19: The snap shots of the X-ray surface brightness (contours) overlaid with emissivity-weighted temperature distribution (gray scale) seen from the direction perpendicular to the collision axis for a head-on collision between equal mass clusters (Takizawa 1999). Left and right panels show plasma mean temperature and electron temperature distribution, respectively.
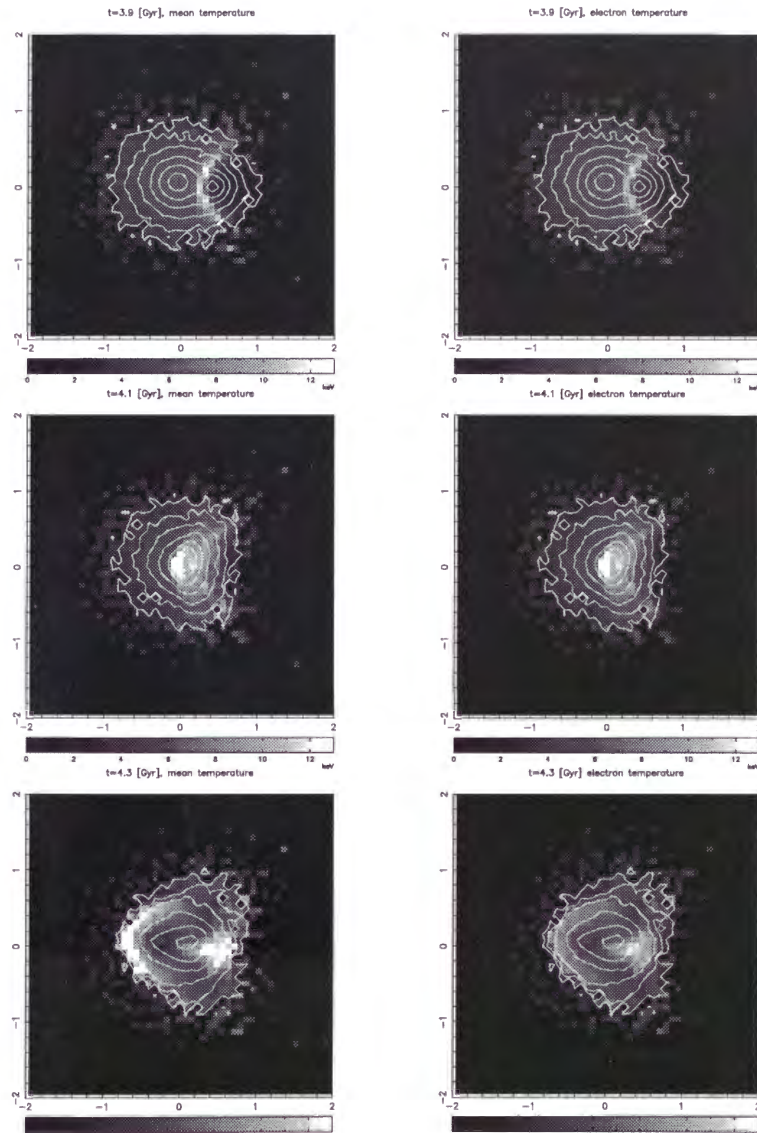
Figure 20: Same as figure 19, but for an absorption of a smaller cluster by a larger one (Takizawa 1999).

62

References

[1] Anninos, P., & Norman, M. L. 1996, ApJ, 459. 12

[2] Arnaud, M., & Evrard, A. E. 1998, submitted to MNRAS, astro-ph/9806353

[3] Bertschinger, E. 1985, ApJS, 58, 39

[4] Binney, J., & Cowie, L. 1981, ApJ, 247, 464

[5] Binney, J., & Tremaine, S. 1987, Galactic Dynamics (Princeton: Princeton University Press)

[6] Binney, J., & Quinn, T. 1991, MNRAS, 249, 678

[7] Bryan, G. L., Cen, R., Norman, M. L., Ostriker, J. P., & Stone, J. M. 1994, ApJ, 428, 405

[8] Bryan, G. L., & Norman, M. L. 1997, in Computational Astrophysics, Proc. 12th Kingston Conference, eds. D Clarke & M. West (PASP), astro-ph/9710186

[9] Burke, D. J., Collins, C. J., Sharples, R. M., Romer, A. K., Holden, B. P., & Nichol, R. C. 1997, ApJ, 488, L83

[10] Cavaliere, A., & Fusco-Femiano, R. 1976, A&A, 49, 137

[11] Cavaliere, A., Menci. N., & Tozzi, P. 1997, ApJ, 484, L21

[12] Cen, R., & Ostriker, J. P. 1994, ApJ, 429, 4

[13] Chiéze, J.-P., Alimi, J.-M, & Teyssier, R. 1998, ApJ, 495, 630

[14] Churazov, E., Gilfanov, M., Forman, W., & Jones, C. 1998, ApJ, submitted, astro-ph/9802166

[15] Collins, C. A., Burke, D. J., Romer, A. K., Sharples, R. M., & Nichol, R. C. 1997, ApJ, 479, L117

[16] Davis, D. S. & White III, R. E. 1998, ApJ, 492, 57

[17] Donnelly, R. H., Markevitch, M., Forman, W., Jones, C., David, L. P., Churazov, E., & Gilfanov, M. 1998, ApJ, 500, 138

[18] Ebeling, H., Edge, A. C., Fabian, A. C., Allen, S. W., Crawford, C. S., & Böhringer, H. 1997, ApJ, 479, L101

[19] Edge, A. C., & Stewart, G. C. 1991, MNRAS, 252, 414

[20] Eke, V. R., Navarro, J. F., & Frenk, C. S. 1998, ApJ, 503, 569

[21] Ettori, S. & Fabian, A. C. 1998, MNRAS, 293, L33

[22] Evrard, A. E. 1990, ApJ, 363, 349

[23] Fabian, A. C. 1994, ARA&A, 32, 277

[24] Fabricant, D. G., Kent, S. M., & Kurtz, M. J. 1989, ApJ, 336, 77

[25] Fox, D. C., & Loeb, A. 1997, ApJ, 491, 459

[26] Fujita, Y., Koyama, K., Tsuru, T., & Matsumoto, H. 1996, PASJ, 48, 191

[27] Funato, Y., Makino, J., & Ebisuzaki, T. 1992a, PASJ, 44, 291

[28] Funato, Y., Makino, J., & Ebisuzaki, T. 1992b, PASJ, 44, 613

[29] Gunn, J. E., & Gott, J. R. 1973, ApJ, 176, 1

[30] Hattori, M., Ikebe, Y., Asaoka, I., Takeshima, Y., Boehringer, H., Mihara, T., Neumann, D. M., Schindler, S., Tsuru, T. & Tamura, T. 1997, Nature, 388, 146

[31] Hénon, M. 1964, Ann. Astrophys., 27, 83

[32] Hirsch, C. 1990, Numerical Computation of Internal and External Flows Vol.2: Computational Methods for Inviscid and Viscous Flows (New York: John Wiley & Sons)

[33] Hoffman, Y., & Ribak, E. 1991, ApJ, 380, L5

[34] Honda, H., Hirayama, M., Watanabe, M., Kunieda, H., Tawara, Y., Yamashita, K., Ohashi, T., Hughs, J., P., & Henry, J. P. 1996, ApJ, 473, L71

[35] Inagaki, Y., Suginohara, T., & Suto, Y. 1995, PASJ, 54, 411

[36] Ishizaka, C., & Mineshige, S. 1996, PASJ, 48, L37

[37] Ishizaka, C., 1997 A & SpS, 254, 233

[38] Jing, Y. P., Mo, H. J., Borner, G., & Fang, L. Z. 1995, MNRAS, 276, 417

[39] Kang, H., Cen, R., Ostriker, J. P., & Ryu, D. 1994, ApJ, 428, 1

[40] Katz, N., & White, S. D. M. 1993, ApJ, 412, 455

[41] Kaiser, N. 1986, MNRAS, 222, 323

[42] Kaiser, N. & Squires, G. 1993, ApJ, 404, 441

[43] Kneib, J. D. P., Mellier, Y., Pello, R., Miralda-Escude, J., Le Borgne, J. F., Boehringer, H., & Picat, J. P. 1995, A&A, 303, 27

[44] Lynden-Bell, D. 1967, MNRAS, 136, 101

[45] McKee, C. F., & Cowie, L., L. 1977, ApJ, 215, 213

[46] Markevitch, M., Mushotzky, R., Inoue, H., Yamashita, K., Furuzawa, A., & Tawara, Y. 1996, 456, 437

[47] Markevitch, M. 1996, ApJ, 465, L1

[48] Markevitch, M. 1998, ApJ, 504, 27

[49] Markevitch, M., Sarazin, C. L., & Irwin, J. A. 1996, ApJ, 472,L17

[50] Markevitch, M., Forman, W. R., Sarazin, C. L., & Vikhlinin, A. 1998, ApJ, 503, 77

[51] Metzler, C. A., & Evrard, A. E. 1994, ApJ, 437, 564

[52] Monaghan, J. J. 1992, ARA&A, 30, 543

[53] Mushotzky, R. F., & Loewenstein, M. 1997, ApJ, 481, L63

[54] Mushotzky, R. F., & Scharf, C. A. 1997, ApJ, 482, L13

[55] Nakamura, F. E., Hattori, M., & Mineshige, S. 1995, A&A, 302, 649

[56] Nakamura, S. 1996 Doctor Thesis of Tokyo Institute of Technology

[57] Navarro, J. F., Frenk, C. S., & White, S. D. M. 1995, MNRAS, 275, 720 (NFW)

[58] Ohashi et al 1997, in X-ray Imaging and Spectroscopy of Cosmic Hot Plasmas, ed. Makino, F., & Mitsuda, K. (Tokyo: Universal Academy Press), 49

[59] Padmanabhan, T., 1993, Structure Formation in the Universe (Cambridge: Cambridge University Press)

[60] Peebles, P. J. E. 1980, The Large-Scale Structure of the Universe (Princeton: Princeton University Press)

[61] Peebles, P. J. E. 1982, ApJ, 257, 438

[62] Pen, U. 1998, 498, 60

[63] Perrenod, S. C. 1978, ApJ, 226, 566

[64] Pistinner, S., & Shaviv, G. 1996, ApJ, 459, 147

[65] Pistinner, S., Levinson, A., & Eichler, D. 1996, ApJ, 467, 162

[66] Press, W. H., & Schechter, P. 1974, ApJ, 187, 425

[67] Richstone, D., Loeb, A., & Turner, E. L. 1992, ApJ, 393, 477

[68] Ricker, P., M. 1998, ApJ, 496, 670

[69] Roettiger, K., Loken, C., & Burns, J. B. 1997 ApJS, 109, 307

[70] Roettiger, K., Stone, J. M., & Mushotzky, R. F. 1998, ApJ, 493, 62

[71] Rosati, P., Ceca, R. D., Norman, C., & Giacconi, R. 1998, ApJ, 492, L21

[72] Rosner, R., & Tucker, W. H. 1989, ApJ, 338, 761

[73] Rybicki, G. B., & Lightman. A. P. 1979, Radiative Process in Astrophysics (New York: John Wiley & Sons)

[74] Sarazin, C. L. 1988, X-ray Emission from Clusters of Galaxies (Cambridge: Cambridge University Press)

[75] Schindler, S., & Müller, E. 1993, A&A, 272, 137

[76] Schindler, S. 1996, A&A, 305, 756

[77] Shafranov, V. D. 1957, Soviet Phys. JETP, 5, 1183

[78] Spitzer, L., Jr. 1962, Physics of Fully Ionized Gases (New York: Wiley)

[79] Spitzer, L., Jr. ,& Hart, M., H. 1971, ApJ, 164, 399

[80] Suginohara, T., & Ostriker, J., P. 1998, ApJ, 507, 16

[81] Sunyaev, R. A., & Zel'dovich, Ya. B. 1972, Comm. Astrophys. Sp. Phys. 4, 173

[82] Sunyaev, R. A., & Zel'dovich, Ya. B. 1980, MNRAS, 190, 413

[83] Suto, Y. 1993, Prog. Theor. Phys., 90, 1173

[84] Takizawa, M., & Mineshige, S. 1998a, ApJ, 499, 82

[85] Takizawa, M., & Mineshige, S. 1998b, in The Hot Universe, ed. Koyama, K., Kitamoto, S., & Itoh, M. (Kluwer)

[86] Takizawa, M. 1998, ApJ, 509, 579

[87] Takizawa, M. 1999, ApJ, submitted

[88] Takizawa, M., Inagaki, S., & Hozumi, S. 1999, Prog. Theor. Phys., submitted,

[89] Thomas, P. A., & Couchman, H. M. P. 1992, MNRAS, 257, 11

[90] van de Weygaert, R., & Bertschinger, E. 1996, MNRAS, 281, 84

[91] Walker, T. P., Steigman, G., Schramm, D. N., Olive, K. A., & Kang, H. 1991, ApJ, 376, 51

[92] Yoshikawa, K., Itoh, M., & Suto, Y. 1998, PASJ, 50, 203

[93] Zel'dovich, Ya. B. 1970, A&A, 5, 84